A Millimeter-Wave Non-Magnetic Passive SOI CMOS Circulator Based on Spatio-Temporal Conductivity Modulation

Tolga Dinc, Student Member, IEEE, Aravind Nagulu, Student Member, IEEE, and Harish Krishnaswamy[®], Member, IEEE

Abstract—Linear, time-invariant, passive circuits and systems constructed from conventional materials with symmetric permittivity and permeability tensors are reciprocal. Breaking Lorentz reciprocity enables the implementation of non-reciprocal components, such as gyrators, isolators, and circulators, which find application in numerous wireless communication systems. Non-reciprocal components are traditionally implemented using ferrite materials, which exhibit the Faraday effect under the application of an external magnetic field bias. However, ferrite materials cannot be integrated into CMOS fabrication processes and require an external biasing magnet, and hence are bulky and expensive. Recently, there has been significant research interest in the implementation of non-magnetic non-reciprocal components using temporal modulation, including a fully integrated 25-GHz circulator in a 45-nm SOI CMOS, demonstrating magneticfree passive non-reciprocity on silicon at millimeter waves for the first time. This paper presents a detailed analysis of the millimeter-wave circulator in both time and frequency domains. Millimeter-wave non-reciprocal operation is enabled by the concept of spatio-temporal conductivity modulation, which achieves broadband non-reciprocal gyrator functionality over theoretically infinite bandwidth (BW). When compared with prior approaches based on N-path filters, spatio-temporal conductivity modulation requires only four-phase 50% duty-cycle clocking at frequencies significantly lower than the operation frequency, enabling scaling to millimeter waves. The 25-GHz circulator achieves minimum transmitter (TX)-to-antenna (ANT)/ANT-to-receiver (RX) insertion losses of 3.3 dB/3.2 dB, respectively, with a 1-dB BW of 4.6 GHz. TX-to-RX isolation is 18.3-21.2 dB (limited by the measurement setup) over the same BW. The circulator IC occupies an area of 1.2 mm \times 1.8 mm ($\lambda/8 \times \lambda/6$). The spatiotemporal conductivity modulation concept is readily scalable across frequency and can be an enabler for higher millimeterwave (e.g., 77 GHz) circulators as well as optical isolators.

Index Terms—5G, circulators, CMOS, duplexer, full duplex, gyrators, interference cancellation, isolators, millimeter wave, millimeter-wave radar, monostatic frequency-modulated continuous-wave (FMCW) radar, non-reciprocity, switched circuits, time-varying circuits.

Manuscript received May 11, 2017; revised July 27, 2017; accepted August 18, 2017. Date of publication November 8, 2017; date of current version November 21, 2017. This paper was approved by Guest Editor Chih-Ming Hung. This work was supported in part by DARPA ACT Program under Grant FA8650-14-1-7414, in part by SPAR Program under Grant HR0011-17-2-0007, and in part by the National Science Foundation EFRI Program under Grant 1343282. (Corresponding author: Harish Krishnaswamy.)

The authors are with the Department of Electrical Engineering, Columbia University, New York, NY 10027 USA (e-mail: harish@ee.columbia.edu).

Color versions of one or more of the figures in this paper are available online at http://ieeexplore.ieee.org.

Digital Object Identifier 10.1109/JSSC.2017.2759422

I. INTRODUCTION

THE scaling of silicon technologies has enabled the exploration of silicon-based millimeter-wave circuits and systems for short-range 60-GHz wireless personal area networks [1], [2], now standardized as the IEEE 802.11ad, as well as for automotive radars [3]–[5]. With the next-generation (5G) of cellular communication networks under development, silicon-based millimeter-wave circuits are likely to become even more prevalent in the future.

In the context of 5G wireless networks, a 1000-fold increase in data traffic is projected over the next ten years as demand for wireless network capacity keeps growing exponentially every year [6]. Solutions for delivering the 1000-fold increase in capacity fall into three main categories: deploying smaller cells (especially in urban settings), allocating more spectrum, and improving spectral efficiency of wireless systems [7]. Smaller cells at low carrier frequencies (1–6 GHz) are unlikely to deliver the demanded capacity increase [8]. On the other hand, millimeter-wave spectrum (frequencies over 24 GHz) offers wider (multi-GHz) channel bandwidths, and therefore has gained significant research interest as one of the most promising solutions to address the data traffic demands of 5G [9].

Full duplex is another emergent technology, which has attracted a lot of research attention in recent years [10]–[18]. Compared with the traditional time- or frequency-division duplexing schemes, full duplex can theoretically double the spectral efficiency in the physical layer by simultaneous transmission and reception on the same frequency channel. Furthermore, it paves the way for revolutionizing wireless protocol design and hence can offer many other new benefits in the higher layers.

When combined with full-duplex operation, millimeter-wave links can offer wide bandwidths (BWs) with improved spectral efficiency, improving network capacity. Millimeter-wave full duplex can be an enabler toward the 1000-fold increase in data traffic, especially in millimeter-wave backhaul. Millimeter-wave full duplex can also be useful to extend the link range (e.g., range of the IEEE 802.11ad) through the implementation of full-duplex repeaters. Additionally, in the 5G era, millimeter-wave small-cell 5G base stations are envisioned to communicate with multiple users simultaneously in uplink and downlink. Although the multiple users

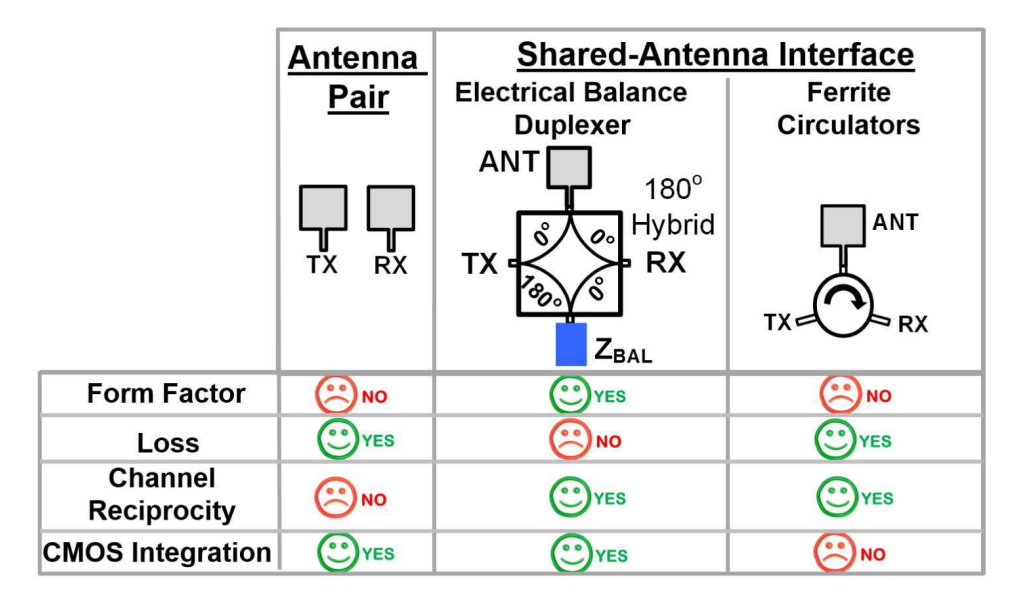


Fig. 1. Tradeoffs associated with conventional full-duplex ANT interfaces.

will occupy adjacent channels in the same band, a low-loss, high-isolation full-duplex antenna (ANT) interface with high power handling capability would be useful to share a single ANT between the transmitter (TX) and the receiver (RX) while eliminating the need for high-quality millimeter-wave diplexers.

Another exciting technology trend is self-driving cars, which will rely on a diverse array of sensor technologies, such as radar, LIDAR, cameras, and ultrasound. Among these sensor technologies, millimeter-wave frequency-modulated continuous-wave (FMCW) radar forms the backbone of automotive sensing, since it can cover short, medium, and long ranges in any weather condition, day or night. A typical monostatic FMCW radar requires a full-duplex ANT interface to share a single ANT between TX and RX.

For all these millimeter-wave applications, a CMOScompatible, low-loss, low-noise full-duplex ANT interface with small form-factor, high linearity, power handling, isolation, and BW is a significant challenge. Among current solutions (Fig. 1), a pair of ANTs is bulky and does not provide channel reciprocity. On the other hand, ferritebased magnetic circulators are not CMOS compatible, leaving passive reciprocal shared-ANT interfaces, such as the electrical balance duplexer (EBD), as the more viable solution. However, it is well known that a three-port reciprocal passive network cannot be lossless, and matched at all ports at the same time. As a result, EBDs [19]–[24] or their microwave counterparts, such as the Wilkinson combiner, suffer from a 3-dB fundamental loss (typically around 4 dB at RF and millimeter wave). In [24], a circular polarization-based EBD is reported with less than 3-dB loss, but it suffers from large form factor $(1.9\lambda \times 1.9\lambda)$, which precludes its use in phased arrays, and more importantly, it uses two ANTs to generate orthogonal polarizations for TX and RX, thus not truly realizing a shared-ANT interface, thus falling into the category of polarization duplexing ANT pairs, such as [25].

This 3-dB theoretical loss can be avoided by breaking Lorentz reciprocity to realize non-reciprocal circulators. Consequently, there has been significant recent interest in breaking reciprocity and realizing circulators in a nonmagnetic IC-compatible fashion using temporal modulation [16], [26]-[29]. In [30], we recently introduced a 25-GHz fully integrated circulator in a 45-nm SOI CMOS enabled by a new concept of spatio-temporal conductivity modulation, marking the first demonstration of magnetic-free passive nonreciprocity at millimeter wave. Spatio-temporal conductivity modulation breaks phase reciprocity similar to the phaseshifted N-path filter of [16] and [29], but features following advantages: 1) it requires modulation or switching at a frequency lower than the operation frequency (1/3rd in this case), enabling operation at millimeter wave; 2) it uses only four 50% duty-cycle I/Q phases, as opposed to numerous low-duty-cycle non-overlapping clocks as in N-path filters, again easing millimeter-wave operation; and 3) it enhances the insertion loss (IL) BW and isolation BW when compared with the N-path-filter-based approach of [16] and [29], since switching is performed across transmission-line delays instead of capacitors as in N-path filters. In principle, since the modulation frequency can be arbitrarily lowered, this first demonstration of a passive non-reciprocal CMOS millimeterwave circulator is scalable in frequency, e.g., to 60 or 77 GHz, upon addressing the additional implementation challenges associated with millimeter-wave design.

This paper presents a detailed discussion of the circulator in [30], including extended time-domain analysis, discussion of the impact of clock imperfections and architectural solutions for the same, circuit descriptions, and extended measurements. This paper is organized as follows. Section II briefly reviews recent advances in non-magnetic circulators based on temporal modulation and describes the proposed spatio-temporal conductivity modulation approach and its associated design tradeoffs. Implementation details of the 25-GHz magnetic-free

passive circulator in 45 a nm SOI CMOS are described in Section III. In Section IV, we present the measurements of the circulator. Section V concludes this paper.

II. SPATIO-TEMPORAL CONDUCTIVITY MODULATION

Any circuit or system that is linear, time-invariant (LTI), passive, and constructed from materials featuring symmetric permittivity and permeability tensors is necessarily reciprocal [31]. Consequently, breaking reciprocity requires violating one of these necessary conditions. Magnetic circulators utilize ferrite materials that become inherently non-reciprocal under the application of an external biasing magnetic field through the Faraday effect [32], but as mentioned earlier, are not compatible with CMOS. Circulators based on active transistors have been extensively explored [33], [34], but the use of active transistors limits the linearity and the noise performance. Non-linearity can be used to violate reciprocity and has been extensively explored in the optical domain [35], [36], but these techniques exhibit non-reciprocity over certain signal power levels only (e.g., larger than 15-dBm input power in [36]) and therefore have limited applicability to wireless applications, which typically demand linearity to the desired signal. Consequently, there has been a strong interest in breaking reciprocity by violating time invariance through time-periodic modulation in recent years (without the use of magnetic materials) [26]-[29].

Prior approaches to non-reciprocity based on temporal modulation have exploited permittivity as the modulated material parameter, specifically spatio-temporal permittivity modulation using varactors in a circuit implementation. However, permittivity modulation is inherently weak due to small modulation index (for example, varactor Cmax/Cmin ratio is typically 2-4 in CMOS), resulting in either large form factors [26] or narrow operation BWs [27]. For example, [26] uses spatio-temporal permittivity modulation in a traveling wave architecture to achieve a direction-dependent frequency conversion along a transmission line. The length of the transmission line required is inversely proportional to the modulation index. Furthermore, it necessitates the use of filters or diplexers to separate the transmitted and received signals. In [27], angular momentum biasing was achieved using spatio-temporal permittivity modulation in a resonant ring. This technique, later demonstrated at microwave frequencies in [28], shrinks the size through the use of lumped LC resonators at the expense of a limited operation BW. Furthermore, permittivity modulation is typically achieved through carrier injection in both varactors and optical modulators [37], [38], resulting in losses (that is, poor varactor quality factors) as the operation frequency is increased to millimeter waves.

On the other hand, conductivity in semiconductors can easily be controlled using transistor switches and enables a modulation index several orders of magnitude larger than permittivity over a wide range of frequencies, including millimeter wave. For example, CMOS transistors exhibit ON-OFF conductance ratios as high as 10^3-10^5 at microwave and millimeter-wave frequencies [39]. Recently, a small form factor, very low-loss, high-isolation and high-linearity RF CMOS passive circulator was demonstrated

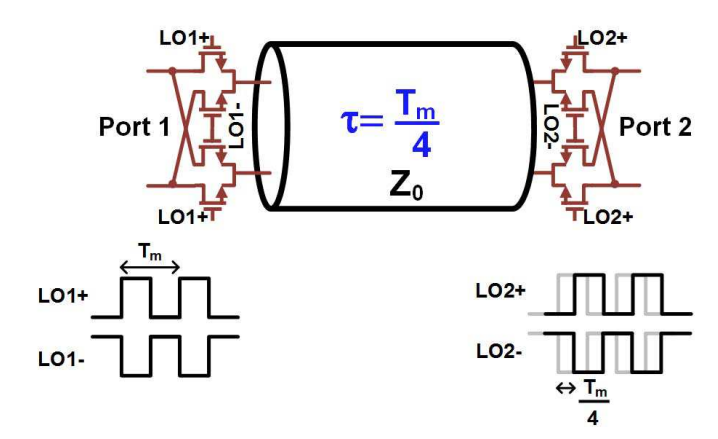


Fig. 2. Proposed spatio-temporal conductivity modulation technique to achieve broadband phase non-reciprocity. Two sets of switches implemented in a fully balanced fashion are placed on either end of a differential transmission line providing a delay equal to one quarter of the modulation period $(T_m/4)$. The modulation clocks of the right switches are delayed with respect to the left ones by the same amount $(T_m/4)$.

in [16] and [29] using phase-shifted N-path filters, essentially a form of spatio-temporal conductivity modulation, as transistors are being switched in a phase-shifted fashion across capacitors. However, N-path filters are not amenable to millimeter-wave operation due to stringent clocking requirements and transistor parasitics. Inspired by the N-path filter-based low-RF CMOS circulator proposed in [16] and [29], we propose a novel generalized concept of spatio-temporal conductivity modulation to achieve wideband millimeter-wave non-reciprocity.

The spatio-temporal conductivity modulation concept consists of two sets of switches implemented in a fully balanced fashion on either end of a differential transmission line delay, as shown in Fig. 2. The switches are modulated between short and open circuit states through periodic square pulses with a 50% duty cycle. The transmission line provides a delay equal to one quarter of the modulation period $(T_m/4)$, and the modulation of the right switches is delayed with respect to those on the left by the same amount $(T_m/4)$. Adding this delay between the two sets of switches allows incident signals from different directions to follow different paths, breaking reciprocity. Fig. 3 shows the signal propagation in the forward direction (from left, or port 1, to right, or port 2). During the first half period of the modulation clock [Fig. 3(a)], when LO1+ is high, the incident signal goes into the transmission line, gets delayed by the transmission line delay of $T_m/4$, and reaches the second set of switches. At this instant, LO2+ is high, so that the signal directly passes to the output. A similar explanation holds also for the second half period of the modulation clock [Fig. 3(b)]: the signal goes into the transmission line with a sign flip and gets delayed by $T_m/4$, and the sign flip is recovered by the second set of switches. In other words, signals traveling in the forward direction experience no polarity inversion in the first half cycle, and two polarity inversions that negate each other in the second half cycle. Thus, effectively, in the forward direction, signals pass through the structure without any loss and experience a delay of one quarter of the modulation period. This can be immediately described by the time-domain equation $v_2^-(t) = v_1^+(t - T_m/4)$,

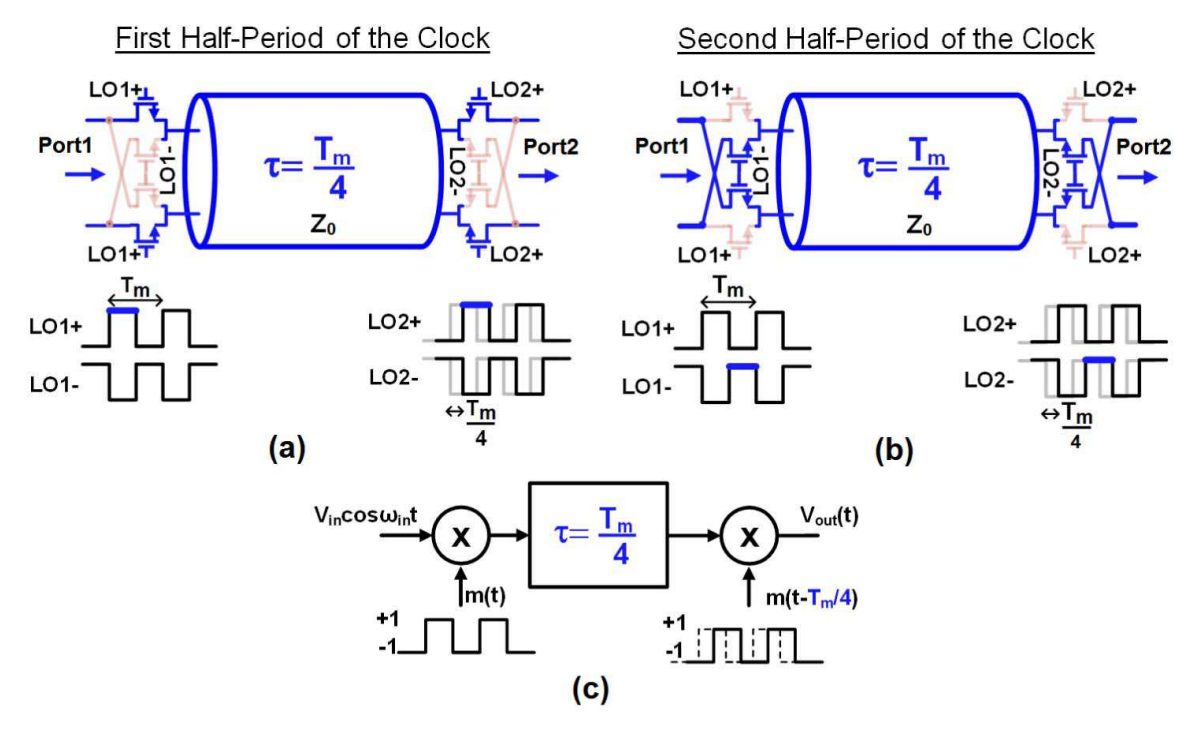


Fig. 3. Signal propagation in the forward direction through the spatio-temporal conductivity modulation structure. (a) First half period of the clock. (b) Second half period of the clock. (c) Signal flow diagram for time-domain analysis. The incident signal passes through the structure without any loss and experiences a transmission line delay of $T_m/4$.

where v_1^+ and v_2^- are the incident and transmitted signals at ports 1 and 2, respectively. Alternatively, this structure can be modeled by multiplication, delay, and multiplication as shown in Fig. 3(c). Here, fully balanced switching operation is modeled as multiplication by a 50% duty-cycle clock, m(t), flipping between +1 and -1. Thus, the output signal can be written as

$$v_2^-(t) = v_1^+(t - T_m/4)m(t - T_m/4)m(t - T_m/4)$$

= $v_1^+(t - T_m/4)$ (1)

which takes advantage of the fact that $m(t - T_m/4)$ $m(t - T_m/4) = +1$ for a binary (-1, +1) signal.

The signal propagation in the backward direction (from right to left) is shown in Fig. 4. During the first half period of the modulation clock, when LO2+ is high, the signal goes into the transmission line and gets delayed by $T_m/4$, and the second set of switches flips the signal sign. Similarly, during the second half period of the modulation clock (LO2- is high), the signal goes into the transmission line with a sign flip, gets delayed by $T_m/4$, and reaches the output as LO1+ is high. In brief, signals traveling from right to left experience a transmission line delay of $T_m/4$ and a polarity inversion in both half cycles. This can be immediately described by $v_1^-(t) = -v_2^+(t - T_m/4)$, where v_2^+ and v_1^- are the incident and transmitted signals at ports 2 and 1, respectively. An analysis based on the signal flow diagram in Fig. 4(c) gives

$$v_1^-(t) = v_2^+(t - T_m/4)m(t - T_m/2)m(t) = -v_2^+(t - T_m/4)$$

which takes advantage of $m(t - T_m/2)m(t) = -1$ for a binary (-1, +1) 50% duty-cycle signal. From (1) and (2),

the resultant S-parameters can be written as

$$S_{21}(\omega_{\rm in}) = +e^{-j\frac{\pi}{2}\left(\frac{\omega_{\rm in}}{\omega_m}\right)} \tag{3}$$

$$S_{12}(\omega_{\rm in}) = -e^{-j\frac{\pi}{2}\left(\frac{\omega_{\rm in}}{\omega_{m}}\right)} \tag{4}$$

where $\omega_{\rm in}$ and ω_m are the signal and modulation frequencies, respectively. It should be noted that $S_{11} = S_{22} = 0$, since there is a pair of switches which connects the transmission line to the input and output at any instant in both half cycles. As can be seen from (3) and (4), this generalized spatio-temporal conductivity modulation technique is ideally lossless and breaks phase reciprocity over a theoretically infinite BW. More importantly, it operates as an ideal passive lossless gyrator-a basic non-reciprocal component postulated by Tellegen [40] that provides a non-reciprocal phase difference of π and can be used as a building block to construct arbitrarily complex nonreciprocal networks—over theoretically infinite BW. It should also be emphasized that although this gyrator is linear and periodically time varying, it contains absolutely no harmonic conversion at its ports, and therefore appears LTI from an external operation perspective. In practice, as shown in Fig. 5, the IL would be limited by ohmic losses in the switches and transmission line, and BW by dispersion effects in the transmission line, particularly if it is implemented in a quasidistributed fashion to absorb the capacitive parasitics of the switches.

A. Insertion Loss, Power Consumption, and Area Versus Modulation Frequency

Fig. 6(a) shows the forward and reverse insertion phases ($\angle S_{21}$ and $\angle S_{12}$, respectively) across frequency

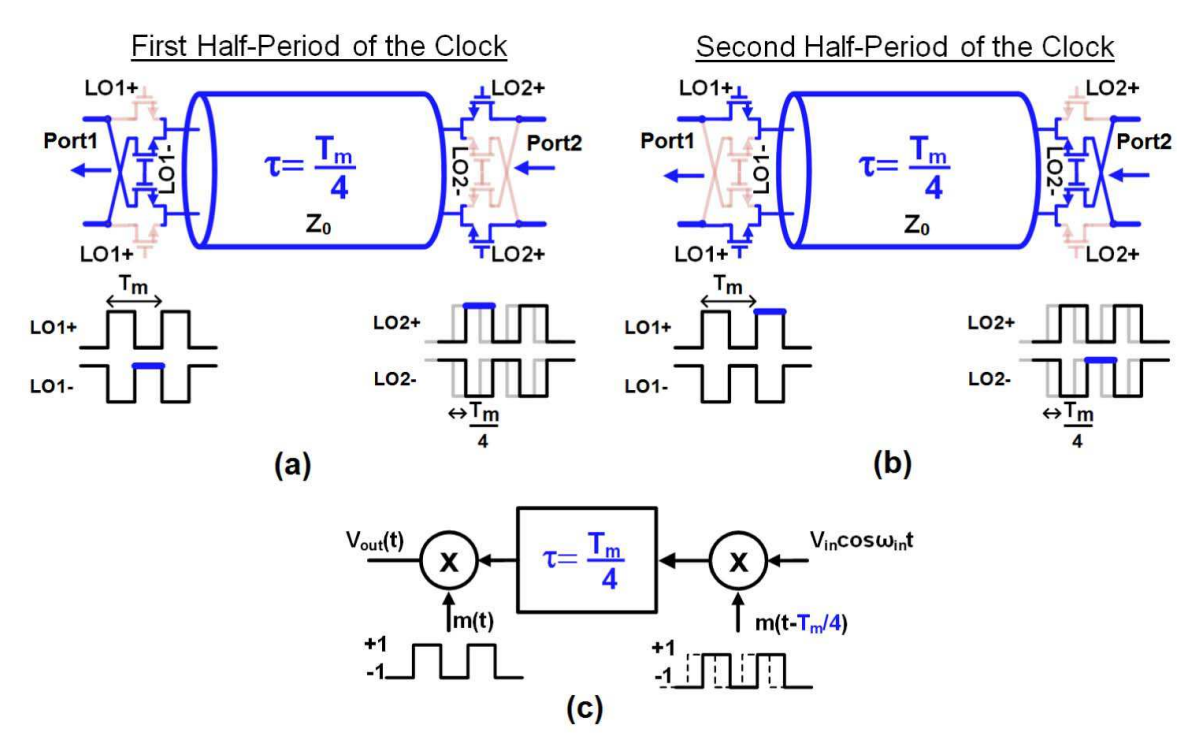


Fig. 4. Signal propagation in the backward direction through the spatio-temporal conductivity modulation structure. (a) First half period of the clock. (b) Second half period of the clock. (c) Signal flow diagram for time-domain analysis. Incident signal experiences no loss, a transmission line delay of $T_m/4$, and a sign flip.

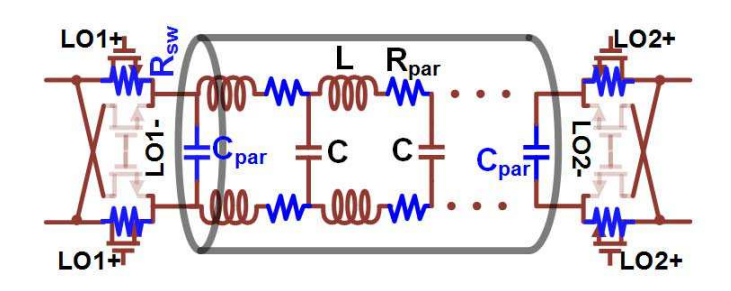


Fig. 5. Ohmic losses in the switches $(R_{\rm SW})$ and transmission line $(R_{\rm par})$, and dispersion effects in the transmission line due to quasi-distributed implementation to absorb the capacitive parasitics of the switches $(C_{\rm par})$ degrade the IL and BW in practice.

normalized to the modulation clock frequency. Achieving $+90^{\circ}$ and -90° phase shifts is important to build the circulator using the ring configuration in [16] and [29], although it should be mentioned that other circulator architectures are certainly possible that exploit an arbitrary forward insertion phase. As can be seen, the spatio-temporal conductivity modulation provides a phase shift of $\pm 90^{\circ}$ at the odd multiples of the modulation frequency, namely $\omega_{in} = (2n - 1)\omega_m$, where n is a positive integer. Fig. 6(b) plots IL and power consumption tradeoffs associated with selecting the modulation frequency (ω_{in}/ω_m) . The real 45-nm SOI CMOS devices augmented with resistive and capacitive layout parasitics are used in this simulation. The final three-stage self-biased inverter buffers are included in the simulation to capture the rise and fall times and dynamic power consumption accurately. A broadband R-L-C model is used for the transmission lines. Using higher odd multiples reduces the clock frequency,

which eases clock generation, distribution, and reduces power consumption. Assuming that a rise and fall time (T_r) up to $T_m/12$ can be tolerated (resulting in 0.8-dB loss, based on simulations), the BW of the square wave can be estimated as BW = $0.35/(T_r)$ = $4.2 f_m$ [41]. Therefore, a modulation frequency of 25 GHz will require designing a clock path with 105-GHz BW compared with a 35-GHz BW for an 8.33-GHz clock, which is more manageable in CMOS processes. Hence, the graph in Fig. 6(b) considers $(\omega_{in}/\omega_m) = 3$ and higher odd multiples. On the other hand, the delay required from the transmission line increases proportionally with $\omega_{\rm in}/\omega_m$, resulting in higher IL¹ and a linearly increasing chip area. Considering all these tradeoffs, we chose an operation to modulation frequency ratio of 3 ($f_m = f_{in}/3 = 8.33$ GHz) not to increase the loss and area significantly while easing the clock generation compared with $f_m = 25$ GHz. In case high-quality transmission lines are available (e.g., transmission lines implemented on package), a lower clock frequency can be selected to lower power consumption. For example, by implementing the transmission lines on the Rogers 4350B substrate (0.02-dB/mm loss at 25 GHz), the clock frequency can be lowered to 1 GHz (using $\omega_{\rm in} = 25\omega_m$) for a similar loss (assuming 0.5-dB loss from the chip-to-package transition).

B. Impact of Clock and Transmission Line Imperfections

Due to modeling errors (in the process development kit or in EM simulations) as well as process and temperature variations,

 1 It should be noted that this represents the loss of the gyrator alone, and the loss of the circulator is in general less than the loss of the gyrator embedded in it.

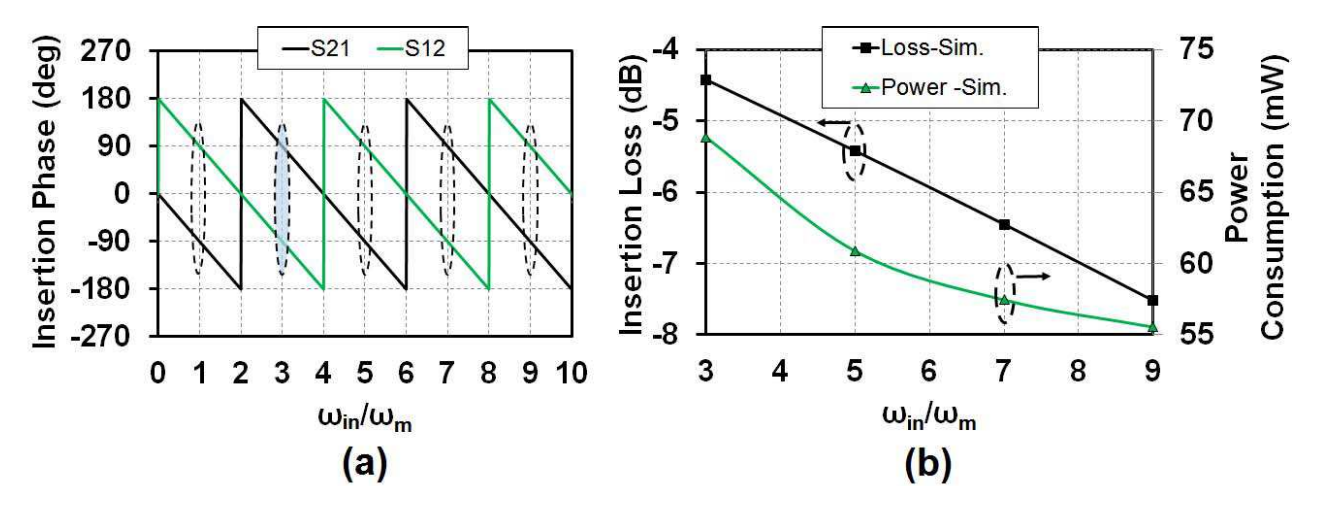


Fig. 6. (a) Non-reciprocal phase difference of 180°, or gyrator operation, is observed over a theoretically infinite BW but insertion phases of $\pm 90^{\circ}$ are seen at odd multiples of the modulation frequency. (b) IL and power consumption tradeoffs associated with selecting the modulation frequency (ω_{in}/ω_{m}).

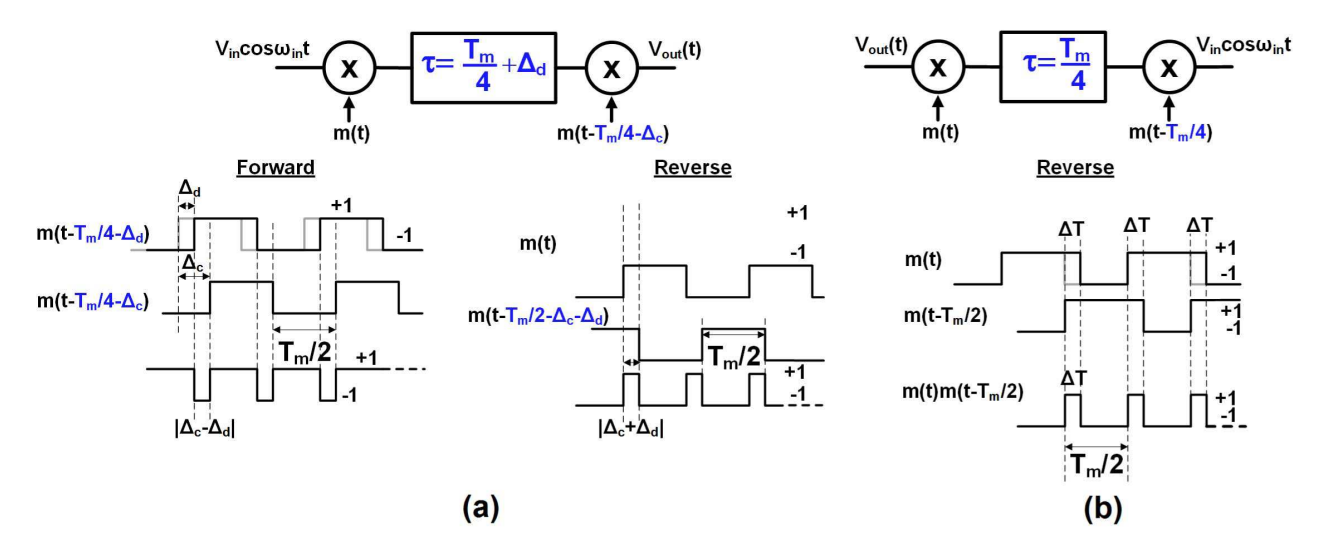


Fig. 7. (a) Impact of transmission line delay errors and clock delay errors on both forward and reverse transmissions. (b) Impact of duty-cycle impairments on the reverse transmission.

the transmission line delay and the delay of the second set of switches can deviate from $T_m/4$, as shown by Δ_l and Δ_c , respectively, in Fig. 7(a). With these delay variations, in the forward direction, $m(t-T_m/4-\Delta_l)m(t-T_m/4-\Delta_c)$ results in a pulse train with a pulsewidth of $|\Delta_c-\Delta_l|$ instead of +1. Similarly, in the reverse direction, $m(t)m(t-T_m/2-\Delta_c-\Delta_l)$ will give a pulse train with a pulsewidth of $|\Delta_c+\Delta_l|$. Thus, $S_{21,i}$ and $S_{12,i}$ (i stands for imperfection) at the operating frequency can be expressed as

$$S_{21,i}(\omega_{\rm in}) = \left(+1 - \frac{4|\Delta_c - \Delta_l|}{T_m}\right) e^{-j\frac{\pi}{2}\left(\frac{\omega_{\rm in}}{\omega_m}\right)} \tag{5}$$

$$S_{12,i}(\omega_{\rm in}) = \left(-1 + \frac{4|\Delta_c + \Delta_l|}{T_m}\right) e^{-j\frac{\pi}{2}\left(\frac{\omega_{\rm in}}{\omega_m}\right)}.$$
 (6)

From (5) and (6), we conclude that small variations in the transmission line and clock delay mainly cause loss, as some portion of the power would be transferred to mixing frequencies due to the harmonic content in the pulse train. For example, a total variation of $|\Delta_c - \Delta_l| = T_m/20$ or

 $|\Delta_c + \Delta_l| = T_m/20$ will result in a loss of ≈ 2 dB in the forward and reverse directions, respectively. Tunability in the transmission line design and clock generation scheme can be incorporated to recover the loss. More importantly, (5) and (6) show that small delay variations do not have any effect on the non-reciprocal phase shift of π (as long as $|\Delta_c - \Delta_l|$ and $|\Delta_c + \Delta_l|$ are less than $T_m/4$).

Duty-cycle impairment in the modulation clock is another imperfection that can have an adverse effect on the operation. Let us assume a deviation from ideal 50% duty cycle, say by ΔT . A similar analysis reveals that the forward direction remains unaffected, since $m(t-T_m/4)m(t-T_m/4)$ continues to be +1, but in the reverse direction, $m(t-T_m/2)m(t)$ will give a pulse train with a pulsewidth of ΔT and a period of $T_m/2$, as shown in Fig. 7(b). Thus, deviation from 50% duty cycle would result in loss in the reverse direction. S_{12} at the operating frequency becomes

$$S_{12,i}(\omega_{\rm in}) = \left(-1 + \frac{4|\Delta T|}{T_m}\right) e^{-j\frac{\pi}{2}\left(\frac{\omega_{\rm in}}{\omega_m}\right)}.$$
 (7)

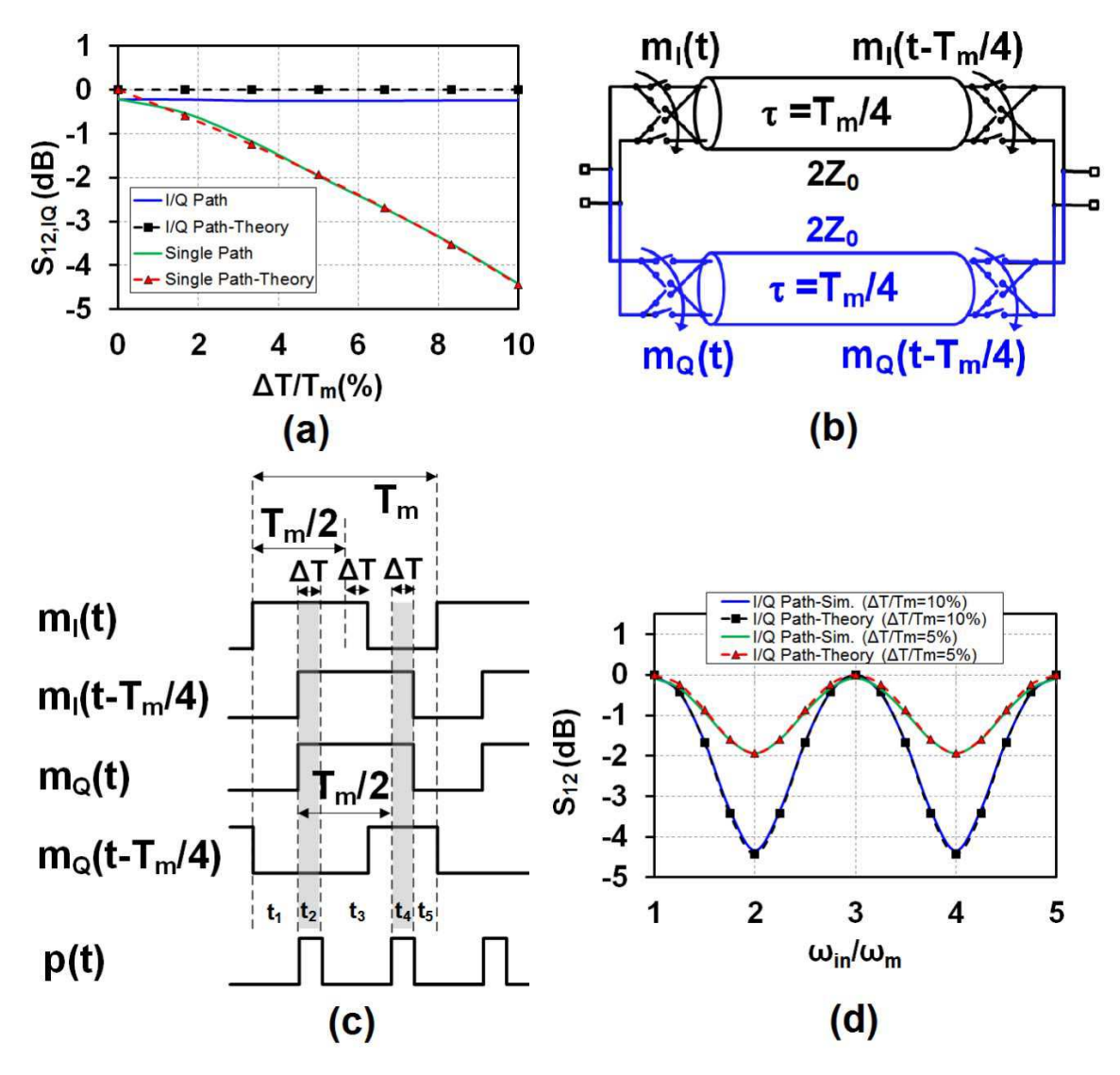


Fig. 8. (a) Theoretical and simulated effect of deviation of the modulation clock from 50% duty cycle (ΔT) for $\omega_{\rm in}=3\omega_m$. Adding a quadrature path mitigates the effect of duty-cycle impairment, ensuring robust operation. (b)Block diagram of the gyrator with the quadrature path added. (c) Clock signals for the gyrator with the quadrature path added, including duty-cycle error. (d) Theoretical and simulated effect of deviation of the modulation clock from 50% duty cycle across frequency for $\Delta T/T_m=0.05$ and $\Delta T/T_m=0.1$. Adding a quadrature path mitigates the effect of duty-cycle impairment at the odd multiples of the modulation frequency.

Fig. 8(a) shows the calculated and simulated IL in the backward direction versus duty-cycle deviation ($\Delta T/T_m$). For example, a deviation from 50% duty cycle to 55% or 45% would degrade the loss by about 2 dB in the reverse direction.

Addition of a quadrature path mitigates the effect of duty-cycle impairment, ensuring a robust operation [Fig. 8(b)]. In this architecture, the characteristic impedance of the transmission lines should be $2Z_0$ for perfect broadband matching. Here, the control of the second sets of switches, $m_Q(t-T_m/4)=m_I(t-T_m/2)$, is generated by inverting $m_I(t)$ (e.g., using $m_Q(t-T_m/4)=\overline{m_I(t)}$). Fig. 8(c) shows the control signals of each set of switches in the I/Q paths with a ΔT deviation from ideal 50% duty cycle. In this structure, the input signal splits evenly into I and Q paths at any time interval. Let us consider the signal flow in a single period. During the time intervals t_1 , t_3 , and t_5 , signals in the I and Q paths pass to output with a delay of $T_m/4$ and a sign flip, adding up. However, during the time intervals t_2 and t_4

which have a duration of ΔT , the signals from the I and Q paths reach the output (port 1) out of phase and thus create a virtual short at the output, reflecting the signals back into the delay lines. These reflected signals travel back and acquire an additional delay of $T_m/4$ and reach port 2 out of phase and reflect again. The reflected signals travel back and reach port 1, but this time they are in phase, passing to the output. Based on this operation, the reverse transmission can be expressed in time domain as

$$v_{1}^{-}(t) = -v_{2}^{+} \left(t - \frac{T_{m}}{4} \right) \left[1 - p \left(t - \frac{T_{m}}{4} \right) \right] + v_{2}^{+} \left(t - \frac{3T_{m}}{4} \right) p \left(t - \frac{3T_{m}}{4} \right)$$
(8)

where p(t) is the pulse train shown in Fig. 8(c). Taking the Fourier transform of the time-domain equation, the reverse

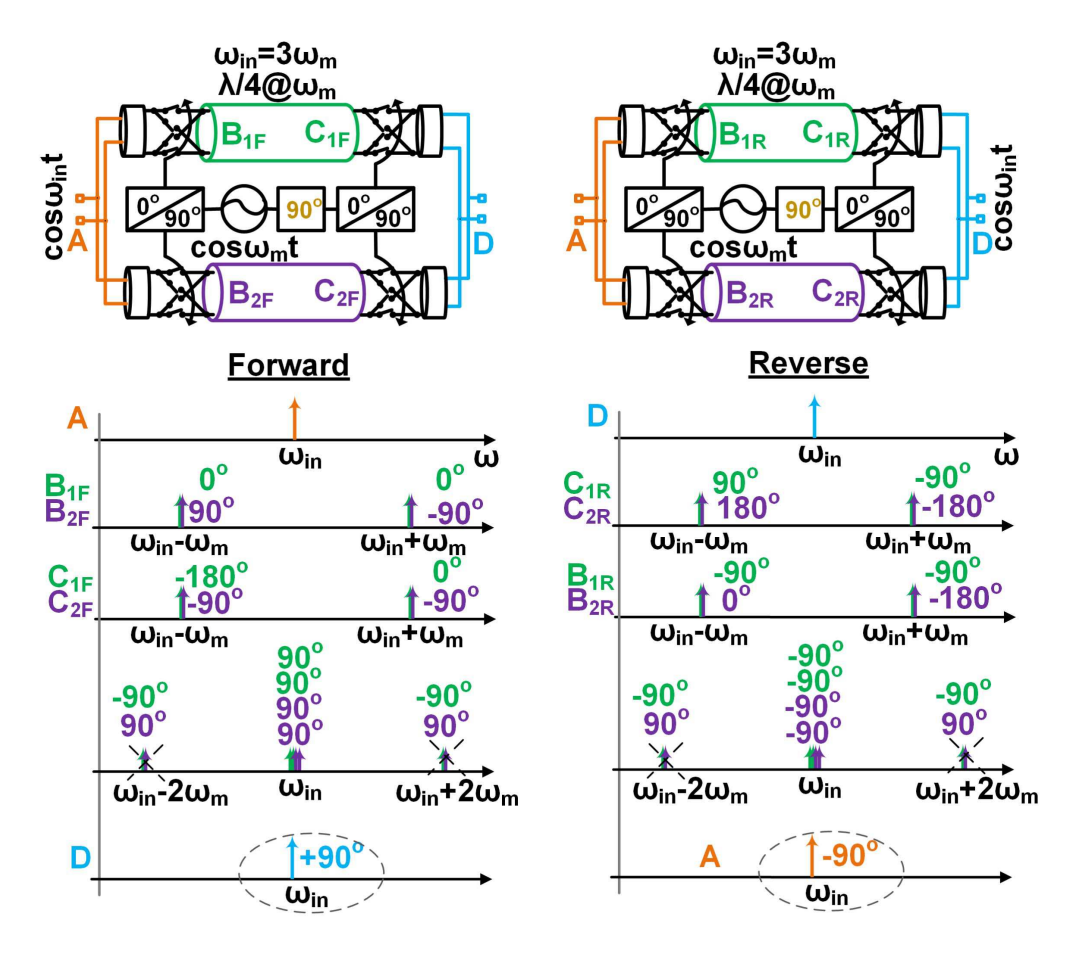


Fig. 9. Simplified frequency-domain mixing-analysis-based explanation of the non-reciprocal phase response of the spatio-temporal conductivity modulation concept.

transmission can be derived in frequency domain as

$$S_{12,IQ}(\omega_{\rm in}) = -e^{-j\frac{\pi}{2}\left(\frac{\omega_{\rm in}}{\omega_m}\right)} \left(1 - \frac{2\Delta T}{T_m} \left[1 + e^{-j\pi\left(\frac{\omega_{\rm in}}{\omega_m}\right)}\right]\right). \tag{9}$$

The term inside the parenthesis goes to +1 at the operating frequency of $\omega_{\text{in}} = 3\omega_m$ (or indeed, any odd multiple of the modulation frequency), thus providing a constant loss of 0 dB in the reverse direction with duty-cycle deviation. Similarly, the transmission in the forward direction can be expressed as

$$S_{21,IQ}(\omega_{\rm in}) = +e^{-j\frac{\pi}{2}\left(\frac{\omega_{\rm in}}{\omega_m}\right)} \left(1 - \frac{2\Delta T}{T_m} \left[1 + e^{-j\pi\left(\frac{\omega_{\rm in}}{\omega_m}\right)}\right]\right)$$
(10)

showing that a similar profile is achieved in the forward direction with a sign flip. Thus, a non-reciprocal phase difference of π is still achieved even in the presence of duty-cycle impairments. Fig. 8(d) shows the simulated and derived S-parameters for different $\Delta T/T_m$ values and across frequency. It should be noted that $S_{12,IQ}$ and $S_{21,IQ}$ change across frequency with duty-cycle deviation, achieving a maximum magnitude of 0 dB and a minimum magnitude of $20\log(1-4\Delta T/T_m)$, the same as the single-path degradation, at operating frequencies that are odd and even multiples of ω_m , respectively. In other words, addition of the Q path recovers the degradation due

to duty-cycle impairment at odd multiples of the modulation frequency, which is where the circulator is designed to operate.

C. Mixer-Delay-Mixer-Based Explanation

The spatio-temporal conductivity modulation operation can also be explained based on a simple frequency-domain mixing analysis (Fig. 9). The I/Q switches commutate the signal at a modulation frequency lower than the operating frequency ($\omega_{\rm in} = 3\omega_m$ in this case). As a result, mixing products appear after the commutation at $\omega_{\rm in} - \omega_m$ and $\omega_{\rm in} + \omega_m$.² These signals flow through the transmission line, which provides -180° and -360° phase shift at $\omega_{\rm in} - \omega_m$ and $\omega_{\rm in} + \omega_m$, respectively (since $\omega_{\rm in}=3\omega_m$). The phase-shifted signals are then commutated again at ω_m but with a phase shift of -90° , creating mixing products at ω_{in} , $\omega_{in} - 2\omega_m$, and $\omega_{in} + 2\omega_m$. The signals at $\omega_{\rm in} - 2\omega_m$ and $\omega_{\rm in} + 2\omega_m$ are 180° out of phase and cancel out. On the other hand, the mixing products at ω_{in} add up constructively into a single signal with perfect lossless transmission and a phase shift of +90°. A similar analysis in the reverse direction shows lossless transmission but a non-reciprocal phase shift of -90°, achieving a nonreciprocal phase shift with 180° difference between forward

²In Fig. 9, we have shown mixing products at $\omega_{\rm in} - \omega_m$ and $\omega_{\rm in} + \omega_m$ for simplicity, but in reality, square-wave commutation will produce mixing products at offsets equal to all odd multiples of ω_m .

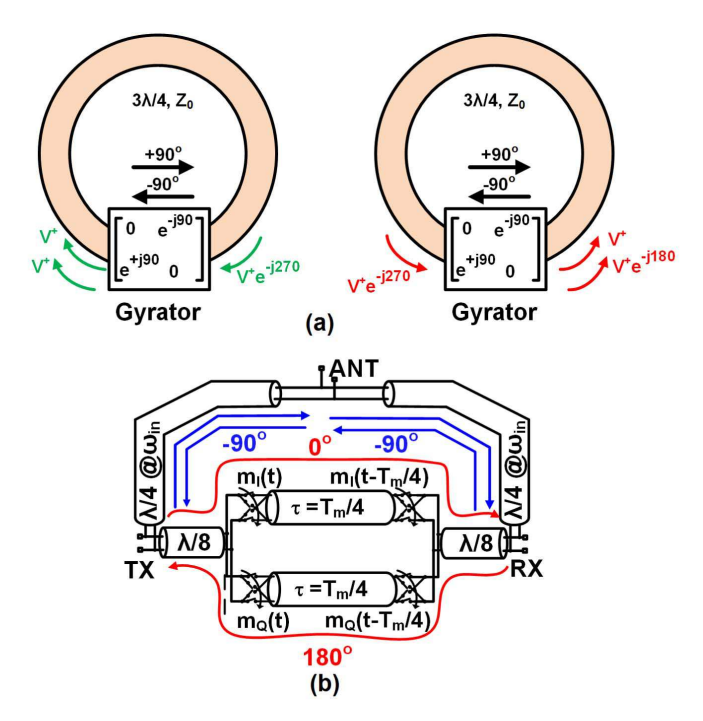


Fig. 10. Circulator architecture. (a) $3\lambda/4$ line is wrapped around the gyrator to support non-reciprocal wave propagation. (b) Circulator is realized by introducing three ports, which are $\lambda/4$ apart. The gyrator is placed symmetrically between the TX and RX ports.

and reverse directions. If there is a mismatch between the electrical lengths of the I and Q transmission lines, the mixing products at $\omega_{\rm in}$ will add up partially, resulting in a loss. The simulated loss remains less than 0.8 dB up to 10% mismatch, with no effect on the non-reciprocal phase shift of π . This mixer-delay-mixer-based explanation sheds insight on the need for broad BW in the transmission lines, as they must support signals at mixing frequencies that are offset from the operating frequency at all odd multiples of ω_m .

III. IMPLEMENTATION

This non-reciprocal phase shift element (gyrator) can now be embedded within a $3\lambda/4$ transmission line ring as shown in Fig. 10(a) to realize a non-reciprocal circulator similar to [29]. In the clockwise direction, the -270° phase shift of the transmission line adds to the -90° phase shift through the gyrator, enabling wave propagation. In the counterclockwise direction, the -270° phase shift of the transmission line adds to the $+90^{\circ}$ phase shift of the gyrator, suppressing wave propagation. A three-port circulator is realized by introducing three ports $\lambda/4$ apart from each other [Fig. 10(b)]. The gyrator is placed symmetrically between the TX and RX ports. The S-parameters of the circulator at $\omega_{\rm in} = 3\omega_m$ can be derived to be

$$S(\omega_{\rm in}) = \begin{pmatrix} 0 & 0 & -1 \\ -j & 0 & 0 \\ 0 & -j & 0 \end{pmatrix}$$
 (11)

through the microwave network analysis, where TX is port 1, ANT is port 2, and RX is port 3.

Fig. 11 shows the implementation of the circulator at 25 GHz. The differential nature of the circulator reduces the local oscillator feedthrough and improves power handling.

The placement of the gyrator in a symmetric fashion between the TX and RX ports enables switch parasitics to be absorbed into the lumped capacitance of the $\lambda/8$ sections on either side, which were implemented using $L_1 = 280$ pH and $C_1 = C_2 = 40$ fF. The fully balanced I/Q quads are designed using $2 \times 16 \mu \text{m}/40 \text{ nm}$ floating-body transistors. Transistor sizes are selected so that the total parasitic capacitance on the either side of the gyrator (C_2) is 40 fF (no physical capacitor is used in the layout). This ensures wideband operation, but limits the switch ON-resistance to $R_{\rm ON}=8.6~\Omega$ (causing \sim 1-dB loss in the circulator). Artificial (quasi-distributed) transmission lines are used in the gyrator, with four stages of lumped π -type C-L-C sections, for size reduction as well as improving IL. Each π -type C-L-C section is essentially a second-order filter with a corner frequency of $\omega_B = 2/\sqrt{2LC}$, referred to as the Bragg frequency, and provides a delay of $\sqrt{2LC}$. Signals at frequencies above the Bragg frequency are strongly attenuated because of an imaginary propagation constant. As mentioned earlier, after the first set of switches, multiple mixing products at $\omega_{\rm in} \pm n\omega_m$ are generated, where n is an odd integer. Mixing products at frequencies higher than Bragg frequency ($\omega_{\rm in} \pm n\omega_m > \omega_B$) will be filtered, forming another loss mechanism. Therefore, it is important to design for a high enough Bragg frequency not to degrade loss significantly. In this paer, L_d and C_d are 200 pH and 20 fF, resulting in a simulated Bragg frequency of 76 GHz. Four π -type C-L-C sections provide a delay of 20 ps and the rest (10 ps) comes from grounded co-planar waveguide transmission lines connecting the inductors together in the layout. Inductors are implemented by stacking two topmost metals (LB and UB) to improve the inductor quality factor (achieving a simulated Q of >20 from 14 to 50 GHz). This improves the circulator loss by 0.3 dB compared with using differential conductor-backed coplanar waveguides. The complete delay-line structure is EM simulated and has an IL of 0.9–2.3 dB from 5 to 50 GHz. The $\lambda/4$ transmission lines between the TX and ANT and ANT and RX ports are implemented using differential conductor-backed coplanar waveguides with a loss of 0.39 dB/mm at 25 GHz. Baluns are included at the TX, ANT, and RX ports to enable single-ended measurements, and separate test structures are included to de-embed the response of the baluns. We envision a fully differential system, including the ANT which can be implemented as a differential microstrip or slot-ring ANT [42], eliminating the need for differential to single-ended conversion. Interested readers can refer to [43] for a single-ended circulator architecture based on the spatiotemporal conductivity modulation concept.

Fig. 12 shows the block and circuit diagrams of the 8.33-GHz LO path. The four-quadrature clock signals driving the switches are generated from two input differential sinusoidal signals at 8.33 GHz. A two-stage poly phase filter (phase imbalance <2° for up to 15% variation in R and C values) is used to generate the 8.33-GHz quadrature signals with 0°/90°/180°/270° phase relationship. After the poly phase filter, a three-stage self-biased CMOS buffer chain with inductive peaking in the final stage generates the square wave clock signals for the switches. Independently controlled NMOS varactors (implemented using $4 \times 40~\mu\text{m}/40~\text{nm}$ floating-body

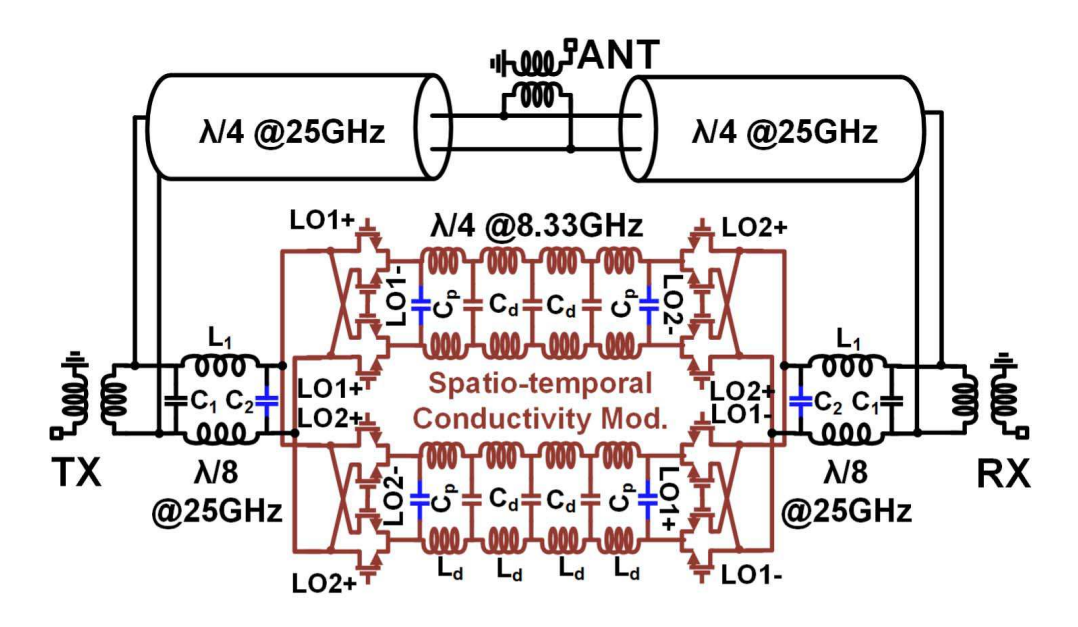


Fig. 11. Circuit diagram of the implemented 25-GHz fully integrated non-reciprocal passive magnetic-free 45-nm SOI CMOS circulator.

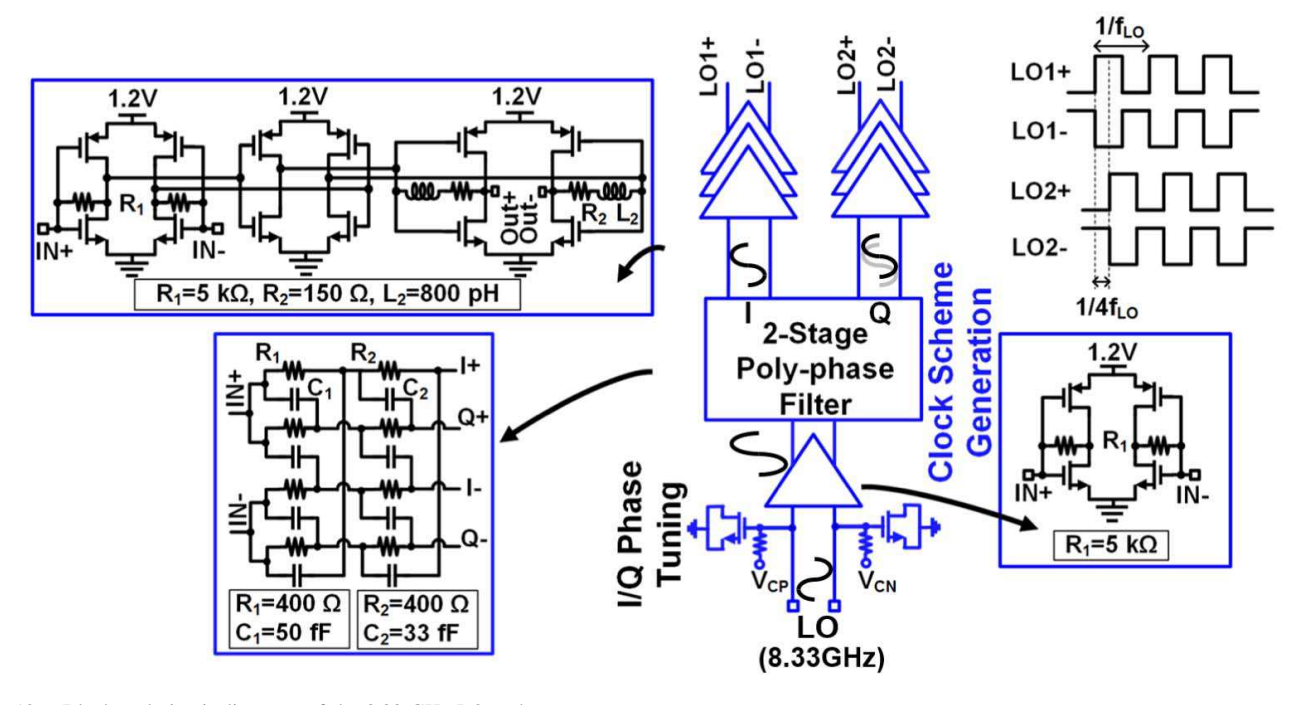


Fig. 12. Block and circuit diagrams of the 8.33-GHz LO path.

devices) are placed at the differential LO inputs to compensate for I/Q imbalance of the poly phase filter. This provides an I/Q calibration range of $\pm 10^{\circ}$ to optimize the circulator performance.

The simulated circulator loss is ~ 3 dB from 23 to 26 GHz [Fig. 13(a)]. In constrast to EBDs, which suffer from fundamental 3-dB loss, the TX-to-ANT and ANT-to-RX IL in this paper are mainly the result of switch ON-resistance, inductor/transmission-line loss due to the finite Q, and dispersion due to the Bragg effect. Fig. 13(b) shows the distribution of circulator loss based on simulations, and it reveals that 34% and 40% of

the total loss come from the switch ON-resistances and finite Q of transmission lines and inductors, respectively. Other loss mechanisms (26%) include finite Bragg frequency as mentioned earlier and clock imperfections. The switch ON-resistance can be reduced by half by removing the quadrature delay-line path and doubling the device sizes, thus preserving the total device parasitic capacitance and, hence, the LO path power consumption. A fine duty-cycle calibration mechanism can be included to counter the impact of duty-cycle impairments. A better technology with lower switch $R_{\rm ON} \times C_{\rm OFF}$ technology constant would also naturally improve the performance. Fig. 13(c) shows the projected

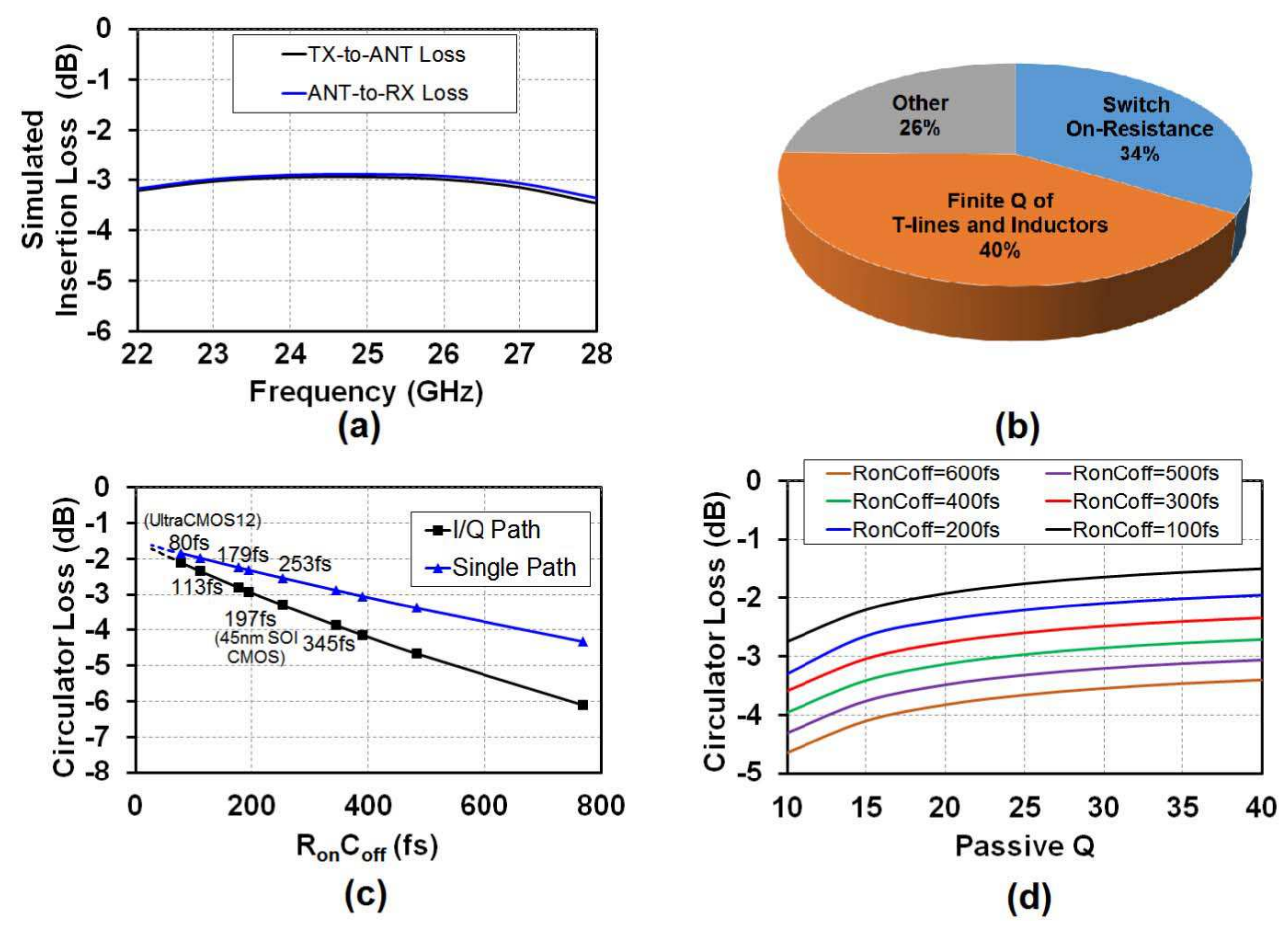


Fig. 13. (a) Simulated circulator IL. (b) Circulator simulated loss distribution: IL is dominated by switch ON-resistance and finite Q of the passives. (c) Projected loss as a function of switch $R_{\rm ON}C_{\rm OFF}$ (the annotated values include 45-nm SOI CMOS and Peregrine's switch technology roadmap, including 80 fs from UltraCMOS12 technology in 2017). Passive Q is assumed to be 20 at 25 GHz. (d) Projected loss in a single path architecture as a function of the passive Q: an IL of less than 2 dB is possible in a technology with lower switch $R_{\rm ON}C_{\rm OFF}$ and/or higher passive Q through a high-resistivity substrate and/or thicker BEOL.

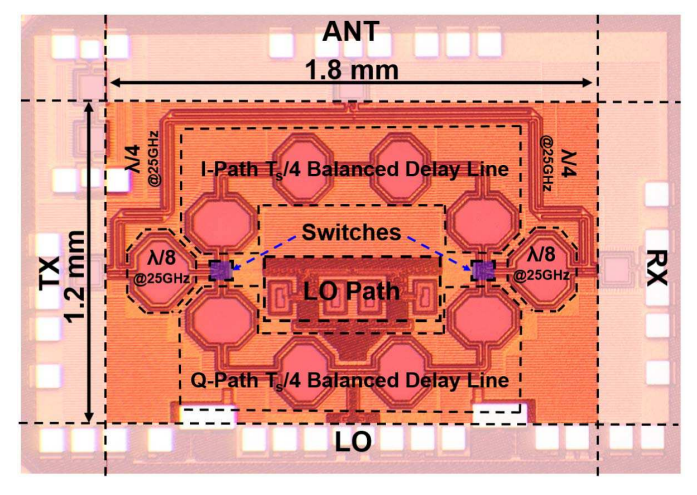


Fig. 14. Chip micro-photograph of the 25-GHz fully integrated non-reciprocal passive magnetic-free 45-nm SOI CMOS circulator based on spatio-temporal conductivity modulation.

loss versus $R_{\rm ON} \times C_{\rm OFF}$ values (based on Peregrine's switch technology roadmap [44] and assuming a passive Q of 20) for two different configurations with the gyrator employing a single path or I/Q paths. Removing the I/Q path would improve the IL by 0.6 dB in this process, and it returns diminishing improvements after that $R_{\rm ON} \times C_{\rm OFF}$ is lower

than 100 fs. Additionally, Fig. 13(d) shows the projected loss for the single-path architecture versus Q for different switch $R_{\rm ON} \times C_{\rm OFF}$ values. For example, an $R_{\rm ON} \times C_{\rm OFF}$ value of 200 fs and Q of 35 (achievable with the high-resistivity substrate and/or thicker back-end-of-line) would enable an integrated circulator with a loss \sim 2 dB. To generate these plots, parasitic resistances in the transmission model and R_{ON} are swept, assuming the same device capacitive parasitics so that they can still be absorbed in the $\lambda/4$ sections. In this process, $R_{\rm ON}$ × $C_{\rm OFF}$ of 2 × 16 μ m/40 nm regular pitch devices is simulated to be \sim 197 fs, including parasitic extraction and EM modeling up to the top metal. This compares well with the simulated $R_{\rm ON} \times C_{\rm OFF}$ of value 185 fs reported in [45] in the same process. $R_{\rm ON} \times C_{\rm OFF}$ is simulated at 75 fs for the intrinsic device model without any extraction, showing that the circulator would also benefit from device layout optimization (e.g., using relaxed pitch devices). Our simulations based on this method differ from measurements by only 0.3 dB, agreeing well.

IV. MEASUREMENTS

The 25-GHz magnetic-free passive circulator is implemented in the global foundries 45-nm SOI CMOS process. Fig. 14 shows a micro-photograph of the circulator IC, which

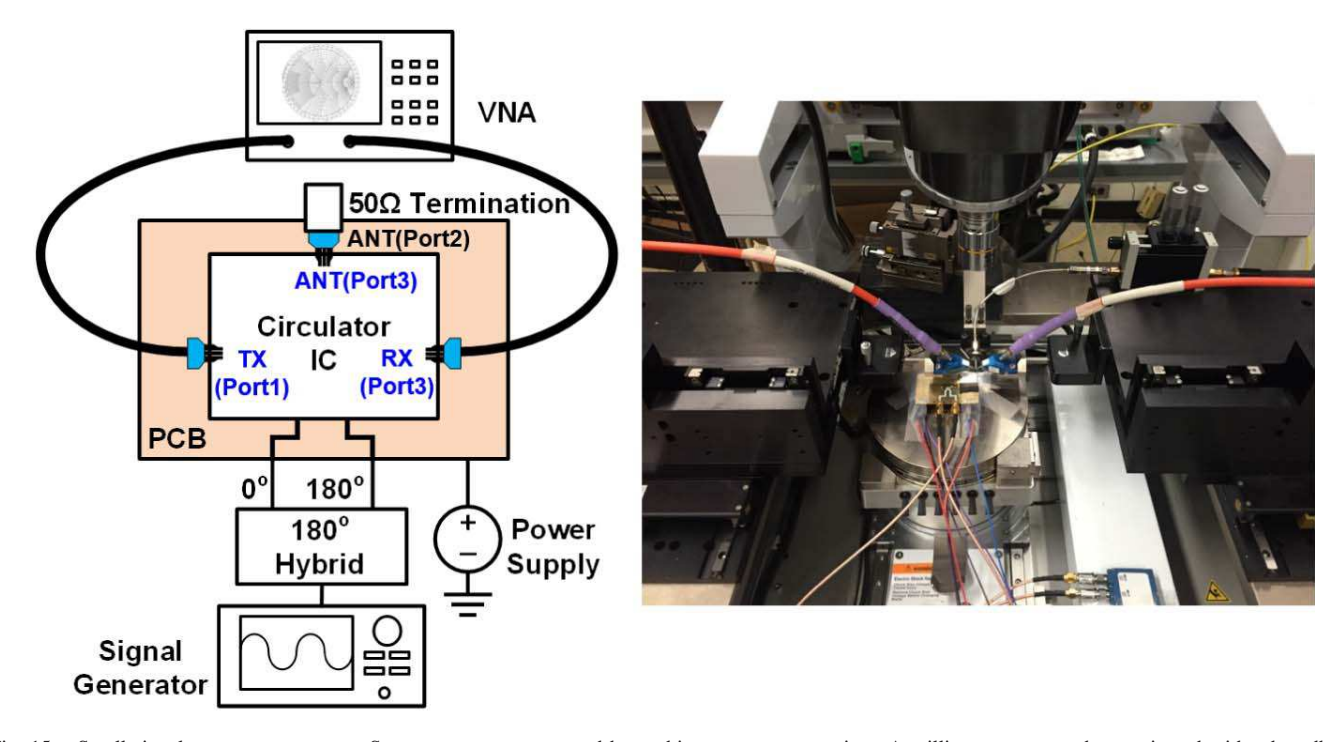


Fig. 15. Small-signal measurement setup: S-parameters are measured by probing two ports at a time. A millimeter-wave probe terminated with a broadband $50-\Omega$ termination is landed on the third port.

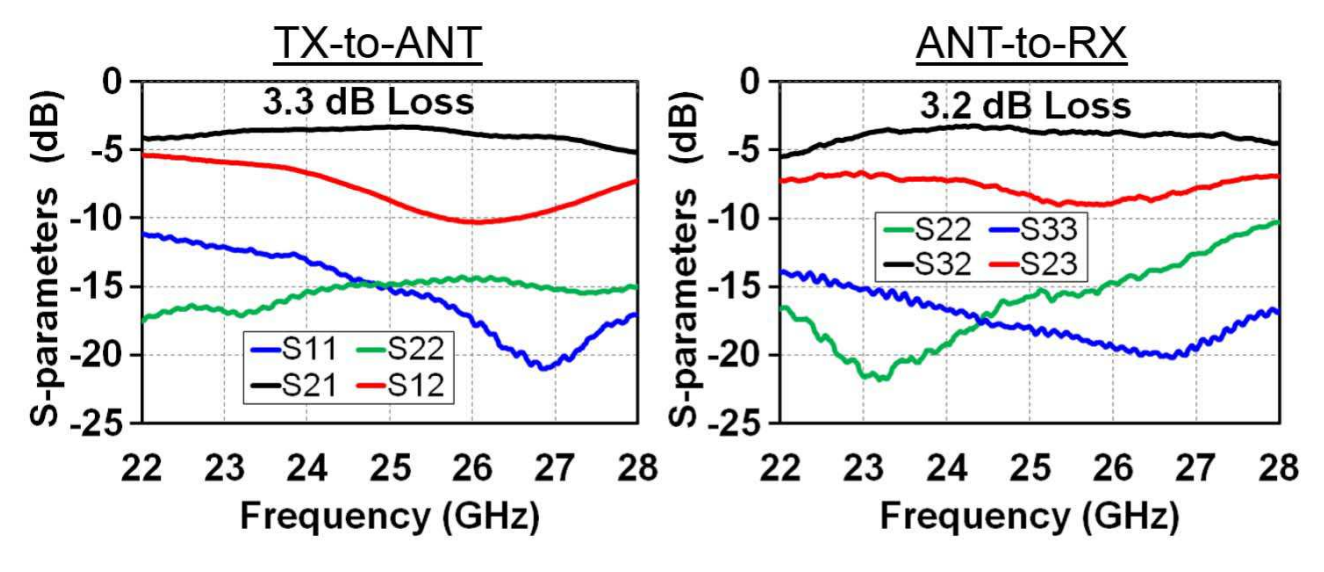


Fig. 16. Circulator TX-ANT and ANT-RX S-parameter measurements for a clock frequency of 8.33 GHz. TX, ANT, and RX are ports 1, 2, and 3, respectively.

occupies 1.2 mm \times 1.8 mm active chip area, excluding the on-chip baluns implemented for testing. S-parameter measurements of the 25-GHz circulator were performed using a setup shown in Fig. 15. The circulator is tested in a chip-on-board configuration through RF probing. DC supply, ground, control voltage, and 8.33-GHz clock input pads are wire bonded to the board. An off-the-shelf 180° hybrid (Krytar 4010265) is used to generate the differential (0°/180°) 8.33-GHz signals from a signal generator to drive the clock inputs of the circulator. A two-port Anritsu 37397E Lightning vector network analyzer is used to measure the S-parameters by probing two ports at a time, while a millimeter-wave probe terminated with a broadband 50- Ω termination is landed on the third port.

When the circulator is configured for clockwise circulation with spatio-temporal conductivity modulation at 8.33 GHz, a broadband non-reciprocal behavior is observed over more than 6-GHz BW (Figs. 16 and 17). The measured transmissions in the clockwise direction (S_{21} , S_{32} , and S_{13}) are -3.3, -3.2, and -8.7 dB, respectively, at 25 GHz. The measured isolation levels in the reverse direction (S_{12} , S_{23} , and S_{31}) are -10.3, -9, and -18.9 dB, respectively, without any port impedance tuning. The circulator is designed to exhibit the best performance for S_{21} , S_{32} , and S_{31} (namely TX-to-ANT loss, ANT-to-RX loss, and TX-to-RX isolation) as these are the most critical parameters in wireless communication and radar applications. The ILs S_{21} and S_{32} degrade by 1 dB over 4.6-GHz BW (18.4%, notably wide-

	TMTT2010 [33]	TMTT2015 [34]	TMTT2016 [23]	JSCC2017 [16]	This work
Technique	Active Quasi Circulator	Active Quasi Circulator	Electrical Balance Duplexer	N-Path-Filter- based Magnetic- Free Passive Circulator	Magnetic-Free Passive Circulator Based on Spatio-Temporal Conductance Mod.
Technology	180nm CMOS	180nm CMOS	180nm SOI CMOS	65nm CMOS	45nm SOI CMOS
Frequency	24GHz	24GHz	1.9-2.2GHz	0.75GHz	22.7-27.3GHz
TX-ANT Transmission	+22.4dB	-5.7dB	-3.7dB	-1.7dB	-3.3dB @ 25GHz (1dB BW 22-27.3 GHz)
ANT-RX Transmission	+12.3dB	-5.7dB	-3.9dB	-1.7dB	-3.2dB @ 24.7GHz (1dB BW 22.7-27.5 GHz)
TX-RX Isolation	>15dB	>20 dB	>40dB	>20dB	>18.5dB ⁵
Isolation BW ¹	~1%	~1.6%	~15%	4.3%	18% ⁶
Center frequency/ Modulation frequency	N/A	N/A	N/A	1	3
Area	3.22mm ²	0.715mm ²	1.75mm ²	0.64mm ² /25mm ² ³	2.16mm ²
ANT-RX NF	17dB	N/R	3.9dB	4.3dB ⁴	3.3-4.4dB
TX-ANT IP1dB	-19.8dBm	+9.5dBm	N/R	N/R	>+21.5dBm
TX-ANT IIP3	-11dBm	N/R	+70dBm	+27.5dBm	+19.9dBm
P _{DC}	144.8mW	7.2mW	0	59mW	78.4mW

TABLE I
PERFORMANCE SUMMARY AND COMPARISON

N/A: Not Applicable, N/R: Not Reported

⁶ This is the 1dB insertion loss BW.

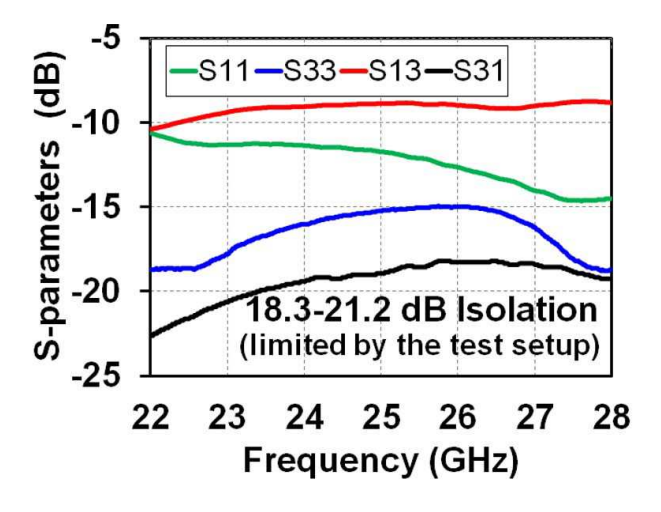


Fig. 17. TX-RX S-parameter measurements. A broadband TX-to-RX isolation of 18.3–21.2 dB over 4.6 GHz (the 1-dB BW of the ILs) is observed, limited by the reflection at the ANT port (a general limitation for all circulators and exacerbated at millimeter wave).

band compared with prior art [29]), and the isolation (S_{31}) over this BW ranges from -18.3 to -20.2 dB (Fig. 17). The circulator power consumption is 78.4 mW. It is dominated by the three-stage buffer at the LO output, consuming 67.8 mW, and the driving amplifier at the LO input consumes 10.6 mW.

It should also be emphasized that the near-20 dB isolation does not represent the fundamental isolation of the circulator,³ but rather is limited by reflections at the ANT port (port 2) due to imperfect termination impedance, a general limitation for all circulators and exacerbated at millimeter wave. As was mentioned earlier, the termination of port 2 is achieved by landing a millimeter-wave probe terminated with a 50- Ω termination impedance. In millimeter-wave measurements, it is challenging to obtain better than 20-dB reflection coefficient from a probe and termination impedance combination. Measurements were performed using an external ANT impedance tuner, as shown in Fig. 18(a). It can be seen that high isolation levels are achievable, but the BW of the isolation is limited by the delay of the cable that connects the probe to the tuner. In practice, achieving higher isolation over wider BWs requires the integration of an ANT impedance tuner on the same chip as the circulator. In Fig. 18(b), simulations are performed using the measured circulator S-parameters, and an on-chip tuner is emulated by directly tuning the impedance at the ANT port. It can be seen that >40-dB isolation is achievable over gigahertz-wide BWs.

The TX-to-ANT/ANT-to-RX input $P_{1 \text{ dB}}$ s are >+21.5/+21 dBm (Fig. 19), respectively (setup limited). They could not be driven into compression due to the

¹ BW over which an isolation better than the value quoted in the row above is maintained.

² Additional 3dB fundamental loss, if signals are not coherent

³ Includes SMD inductors on PCB.

 $^{^4}$ Includes 2.3dB degradation due to LO phase noise.

⁵ Limited by the mmWave test setup.

³In a real system, ANT matching does not only affect the magnitude of isolation but also its BW

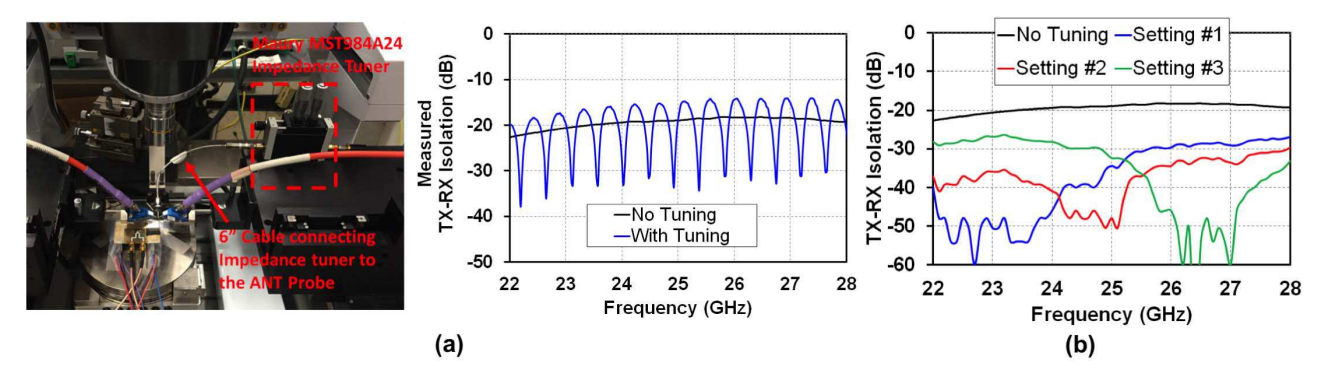


Fig. 18. (a) Measured TX-to-RX isolation using an external ANT impedance tuner. High isolation levels are achieved but the BW of the isolation is limited by the cable that is used to connect to the tuner. (b) Simulated TX-to-RX isolation based on measured circulator S-parameters through direct tuning of impedance at the ANT port.

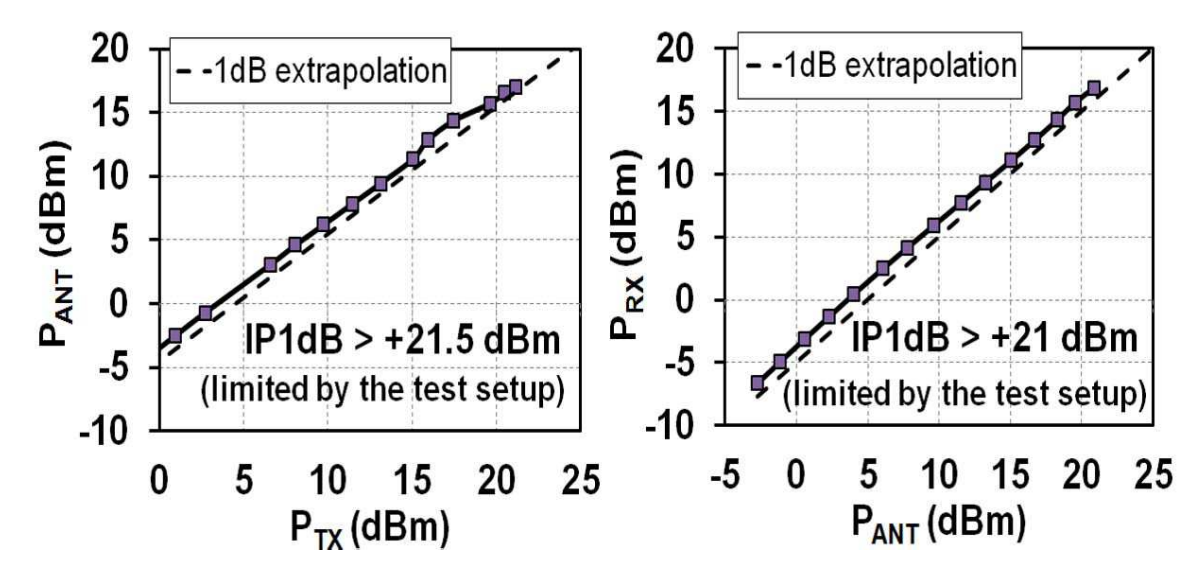


Fig. 19. Circulator TX-to-ANT and ANT-to-RX large-signal measurements: TX-to-ANT input P1 dB is +21.5 dBm, while ANT-to-RX input P1 dB is +21 dBm (limited by the test setup).

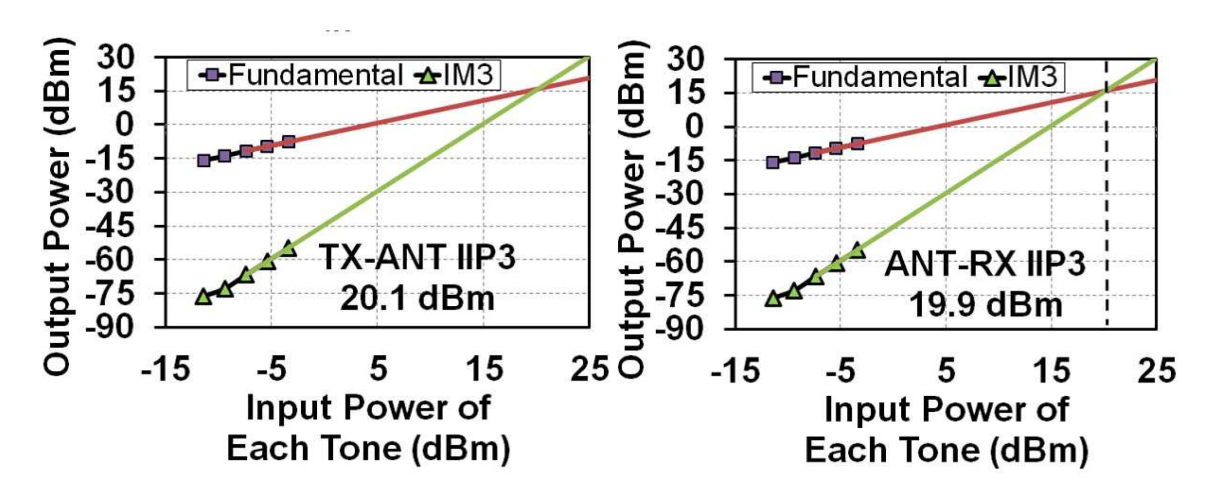


Fig. 20. Measured TX-to-ANT and ANT-to-RX IIP3s.

limited output power of the driving amplifier in the testing setup. The measured TX-to-ANT and ANT-to-RX IIP3s are $\sim +20$ dBm (Fig. 20) using two tones at 25 and 25.1 GHz. It is noteworthy that the $P_{1\,\mathrm{dB}}$ s are high relative to the

IIP3s, because the circulator graceful transitions to reciprocal operation under large-signal operation as switching action is controlled by the large input signal instead of the modulation signal. Since IIP3 is an extrapolation from small-signal levels,

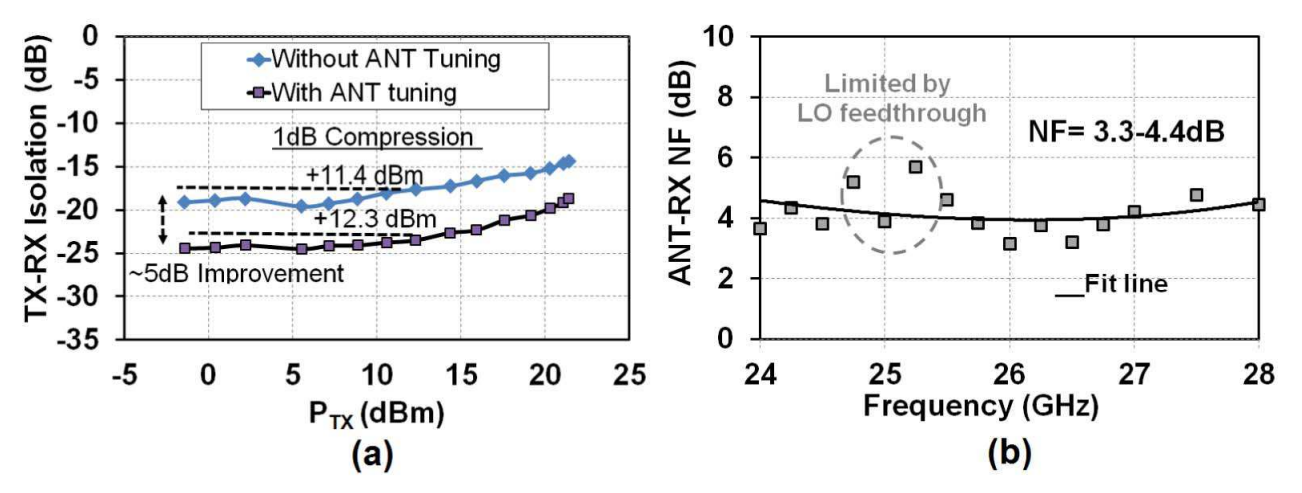


Fig. 21. (a) Measured TX-to-RX large-signal isolation and (b) circulator ANT-RX noise figure. Without ANT tuning, TX-RX isolation compresses by 1 dB at 11.4 dBm and 3 dB at 21.45 dBm. An external ANT impedance tuner enables a higher initial isolation of 25 dB (still limited by the measurement setup) and 1-dB compression at +12.3 dBm. ANT-RX NF is consistent with the IL, showing negligible degradation due to LO phase noise.

this transition is not reflected in IIP3 measurements. The measured TX-to-RX isolation performance versus the transmit power is shown in Fig. 21(a). TX-to-RX Isolation (ISO) compresses by 1 and 3 dB at +11.4 and +21.45 dBm, respectively. This can be compensated by an external ANT impedance tuner, which enables a higher initial small-signal ISO of 25 and 1 dB compression at +12.3 dBm. The measured ANT-RX noise figure (NF) is shown in Fig. 21(b) and ranges from 3.3 to 4.4 dB, consistent with the IL and not degraded by LO phase noise.

Table I compares this circulator with prior art. This circulator performs better than active millimeter-wave circulators [33], [34] in all metrics (loss, linearity, NF, and BW). When compared with a passive EBD [46], this paper achieves >1 dB overall advantage in IL (the sum of TX-to-ANT and ANT-to-RX ILs) while operating at >10 times higher frequency. When compared with the N-path filter-based circulator of [16] and [29], operation at millimeter waves is enabled by the ability to perform modulation at a frequency much lower than the operating frequency using four square-wave clocks with 0°/90°/180°/270° phase shift and 50% duty cycle, as opposed to eight or more non-overlapping clocks with low duty cycle running at the operation frequency as is the case with N-path filters. Furthermore, the proposed conductivity modulation across transmission line delays results in far more broadband non-reciprocity than [29]. N-path switchedcapacitor approaches inherently yield the second-order bandpass filter response with a BW that is directly related to the capacitor value. Such a narrowband filter response is avoided here through the use of transmission line delays that are quarter-wave at the modulation frequency. While such narrowband filtering might be desirable in some applications (for instance, for tolerance of out-of-band interference at RF), other applications, such as millimeter-wave systems, which inherently offer interference tolerance and spatial reuse through beamforming, would benefit from wideband operation. It should also be mentioned that the N-path approach offers the benefit of an ultra-compact, electrically infinitesimal,

inductor-less gyrator implementation, albeit with harmonic conversion effects, unlike the gyrator proposed in this paper.

V. CONCLUSION

This paper presented the first millimeter-wave fully integrated CMOS magnetic-free passive circulator enabled by a novel generalized spatio-temporal conductivity modulation concept. Spatio-temporal conductivity modulation achieves broadband gyrator operation over theoretically infinite BW. The 25-GHz circulator achieves 3.3-dB/3.2-dB TXto-ANT/ANT-to-RX ILs, respectively, with a 1-dB BW of 4.6 GHz. TX-to-RX isolation is 18.3-21.2 dB (limited by the measurement setup) over the 1-dB IL BW. The concept is readily scalable across frequency and can be an enabler for 77-GHz circulators as well as optical isolators. Several topics may be considered for future research. EBDs, such as the one in [23], achieve very high linearity and power handling through the high-linearity static switch design, particularly in SOI CMOS technologies. Incorporation of similar techniques to improve the linearity and power handling of integrated non-reciprocal spatio-temporal modulated circulators is an important research direction. EBDs also feature balance impedances that are able to maintain isolation in the presence of ANT impedance variation, and exploration of such balance networks in spatio-temporal modulated circulators is also an interesting future research topic. Scaling of full-duplex concepts to large-scale phased arrays is another challenge that should be overcome to reveal the true benefits offered by millimeter-wave full duplex.

ACKNOWLEDGMENTS

The authors would like to thank Dr. T. Olsson and Dr. B. Epstein of DARPA and Prof. A. Alu of UT Austin for useful discussions and Global Foundries for chip fabrication donation. They would also like to thank Prof. A. Natarajan of Oregon State University and Prof. K. Bergman and Prof. K. Shepard of Columbia University for equipment support.

REFERENCES

- A. Natarajan et al., "A fully-integrated 16-element phased-array receiver in SiGe BiCMOS for 60-GHz communications," *IEEE J. Solid-State Circuits*, vol. 46, no. 5, pp. 1059–1075, May 2011.
- [2] S. Emami et al., "A 60 GHz CMOS phased-array transceiver pair for multi-Gb/s wireless communications," in *IEEE Int. Solid-State Circuits Conf. (ISSCC) Dig. Tech. Papers*, Feb. 2011, pp. 164–166.
- [3] Y.-A. Li, M.-H. Hung, S.-J. Huang, and J. Lee, "A fully integrated 77 GHz FMCW radar system in 65 nm CMOS," in *IEEE Int. Solid-State Circuits Conf. (ISSCC) Dig. Tech. Papers*, Feb. 2010, pp. 216–217.
- [4] J. Hatch, A. Topak, R. Schnabel, T. Zwick, R. Weigel, and C. Waldschmidt, "Millimeter-wave technology for automotive radar sensors in the 77 GHz frequency band," *IEEE Trans. Microw. Theory Techn.*, vol. 60, no. 3, pp. 845–860, Mar. 2012.
- [5] V. Giannini et al., "A 79 GHz phase-modulated 4 GHz-BW CW radar transmitter in 28 nm CMOS," *IEEE J. Solid-State Circuits*, vol. 49, no. 12, pp. 2925–2937, Dec. 2014.
- [6] J. Zander and P. Mähönen, "Riding the data tsunami in the cloud: Myths and challenges in future wireless access," *IEEE Commun. Mag.*, vol. 51, no. 3, pp. 145–151, Mar. 2013.
- [7] J. G. Andrews et al., "What will 5G be?" IEEE J. Sel. Areas Commun., vol. 32, no. 6, pp. 1065–1082, Jun. 2014.
- [8] Y. Zhu et al., "Demystifying 60 GHz outdoor picocells," in Proc. 20th Annu. Int. Conf. Mobile Comput. Netw., New York, NY, USA, 2014, pp. 5–16.
- [9] B. Sadhu et al., "A 28 GHz 32-element phased-array transceiver IC with concurrent dual polarized beams and 1.4 degree beam-steering resolution for 5G communication," in *IEEE Int. Solid-State Circuits Conf. (ISSCC)* Dig. Tech. Papers, Feb. 2017, pp. 128–129.
- [10] A. Sabharwal, P. Schniter, D. Guo, D. W. Bliss, S. Rangarajan, and R. Wichman, "In-band full-duplex wireless: Challenges and opportunities," *IEEE J. Sel. Areas Commun.*, vol. 32, no. 9, pp. 1637–1652, Sep. 2014.
- [11] D. Bharadia, E. McMilin, and S. Katti, "Full duplex radios," ACM SIG-COMM Comput. Commun. Rev., vol. 43, no. 4, pp. 375–386, Aug. 2013. [Online]. Available: http://doi.acm.org/10.1145/2534169.2486033
- [12] D. Yang, H. Yüksel, and A. Molnar, "A wideband highly integrated and widely tunable transceiver for in-band full-duplex communication," *IEEE J. Solid-State Circuits*, vol. 50, no. 5, pp. 1189–1202, May 2015.
- [13] J. Zhou, T.-H. Chuang, T. Dinc, and H. Krishnaswamy, "Integrated wideband self-interference cancellation in the RF domain for FDD and full-duplex wireless," *IEEE J. Solid-State Circuits*, vol. 50, no. 12, pp. 3015–3031, Dec. 2015.
- [14] D.-J. van den Broek, E. A. M. Klumperink, and B. Nauta, "An in-band full-duplex radio receiver with a passive vector modulator downmixer for self-interference cancellation," *IEEE J. Solid-State Circuits*, vol. 50, no. 12, pp. 3003–3014, Dec. 2015.
- [15] T. Dinc, A. Chakrabarti, and H. Krishnaswamy, "A 60 GHz CMOS full-duplex transceiver and link with polarization-based antenna and RF cancellation," *IEEE J. Solid-State Circuits*, vol. 51, no. 5, pp. 1125–1140, May 2016.
- [16] N. Reiskarimian, J. Zhou, and H. Krishnaswamy, "A CMOS passive LPTV nonmagnetic circulator and its application in a full-duplex receiver," *IEEE J. Solid-State Circuits*, vol. 52, no. 5, pp. 1358–1372, May 2017.
- [17] N. Reiskarimian, M. B. Dastjerdi, J. Zhou, and H. Krishnaswamy, "Highly-linear integrated magnetic-free circulator-receiver for fullduplex wireless," in *IEEE Int. Solid-State Circuits Conf. (ISSCC) Dig. Tech. Papers*, Feb. 2017, pp. 316–317.
- [18] T. Zhang, A. Najafi, C. Su, and J. C. Rudell, "A 1.7-to-2.2 GHz full-duplex transceiver system with >50 dB self-interference cancellation over 42 MHz bandwidth," in *IEEE Int. Solid-State Circuits Conf. (ISSCC) Dig. Tech. Papers*, Feb. 2017, pp. 314–315.
- [19] H. Darabi, A. Mirzaei, and M. Mikhemar, "Highly integrated and tunable RF front ends for reconfigurable multiband transceivers: A tutorial," *IEEE Trans. Circuits Syst. I, Reg. Papers*, vol. 58, no. 9, pp. 2038–2050, Sep. 2011.
- [20] M. Mikhemar, H. Darabi, and A. A. Abidi, "A multiband RF antenna duplexer on CMOS: Design and performance," *IEEE J. Solid-State Circuits*, vol. 48, no. 9, pp. 2067–2077, Sep. 2013.
- [21] M. Elkholy, M. Mikhemar, H. Darabi, and K. Entesari, "Low-loss integrated passive CMOS electrical balance duplexers with singleended LNA," *IEEE Trans. Microw. Theory Techn.*, vol. 64, no. 5, pp. 1544–1559, May 2016.

- [22] S. H. Abdelhalem, P. S. Gudem, and L. E. Larson, "Tunable CMOS integrated duplexer with antenna impedance tracking and high isolation in the transmit and receive bands," *IEEE Trans. Microw. Theory Techn.*, vol. 62, no. 9, pp. 2092–2104, Sep. 2014.
- [23] B. van Liempd et al., "A +70-dBm IIP3 electrical-balance duplexer for highly integrated tunable front-ends," *IEEE Trans. Microw. Theory Techn.*, vol. 64, no. 12, pp. 4274–4286, Dec. 2016.
- [24] C. Lu, M. K. Matters-Kammerer, A. Zamanifekri, A. B. Smolders, and P. G. M. Baltus, "A millimeter-wave tunable hybrid-transformer-based circular polarization duplexer with sequentially-rotated antennas," *IEEE Trans. Microw. Theory Techn.*, vol. 64, no. 1, pp. 166–177, Jan. 2016.
- [25] T. Dinc and H. Krishnaswamy, "A T/R antenna pair with polarization-based reconfigurable wideband self-interference cancellation for simultaneous transmit and receive," in *IEEE MTT-S Int. Microw. Symp. Dig.*, May 2015, pp. 1–4.
- [26] S. Qin, Q. Xu, and Y. E. Wang, "Nonreciprocal components with distributedly modulated capacitors," *IEEE Trans. Microw. Theory Techn.*, vol. 62, no. 10, pp. 2260–2272, Oct. 2014.
- [27] N. A. Estep, D. L. Sounas, J. Soric, and A. Alu, "Magnetic-free non-reciprocity and isolation based on parametrically modulated coupled-resonator loops," *Nature Phys.*, vol. 10, pp. 923–927, Nov. 2014.
- [28] N. A. Estep, D. L. Sounas, and A. Alù, "Magnetless microwave circulators based on spatiotemporally modulated rings of coupled resonators," *IEEE Trans. Microw. Theory Techn.*, vol. 64, no. 2, pp. 502–518, Feb. 2016.
- [29] N. Reiskarimian and H. Krishnaswamy, "Magnetic-free non-reciprocity based on staggered commutation," *Nature Commun.*, vol. 7, Apr. 2016, Art. no. 11217.
- [30] T. Dinc and H. Krishnaswamy, "A 28 GHz magnetic-free non-reciprocal passive CMOS circulator based on spatio-temporal conductance modulation," in *IEEE Int. Solid-State Circuits Conf. (ISSCC) Dig. Tech. Papers*, Feb. 2017, pp. 294–295.
- [31] D. Jalas et al., "What is—And what is not—An optical isolator," Nature Photon., vol. 7, no. 1038, pp. 579–582, Aug. 2013.
- [32] D. M. Pozar, Microwave Engineering, 4th ed. Hoboken, NJ, USA: Wiley, 2011.
- [33] H.-S. Wu, C.-W. Wang, and C.-K. C. Tzuang, "CMOS active quasicirculator with dual transmission gains incorporating feedforward technique at K-band," *IEEE Trans. Microw. Theory Techn.*, vol. 58, no. 8, pp. 2084–2091, Aug. 2010.
- [34] J.-F. Chang, J.-C. Kao, Y.-H. Lin, and H. Wang, "Design and analysis of 24-GHz active isolator and quasi-circulator," *IEEE Trans. Microw. Theory Techn.*, vol. 63, no. 8, pp. 2638–2649, Aug. 2015.
- [35] M. Soljačić, C. Luo, J. D. Joannopoulos, and S. Fan, "Nonlinear photonic crystal microdevices for optical integration," *Opt. Lett.*, vol. 28, no. 8, pp. 637–639, Apr. 2003. [Online]. Available: http://ol.osa.org/ abstract.cfm?URI=ol-28-8-637
- [36] A. M. E. A. Mahmoud, "All-passive nonreciprocal metastructure," Nature Commun., vol. 6, Jul. 2015, Art. no. 8359.
- [37] Q. Xu, S. Manipatruni, B. Schmidt, J. Shakya, and M. Lipson, "12.5 Gbit/s carrier-injection-based silicon micro-ring silicon modulators," *Opt. Exp.*, vol. 15, no. 2, pp. 430–436, Jan. 2007. [Online]. Available: http://www.opticsexpress.org/abstract.cfm?URI=oe-15-2-430
- [38] F. Gardes, G. Mashanovich, and G. Reed. (Dec. 2007). "Evolution of optical modulation in silicon-on insulator devices." SPIE Newsroom. Tech. Rep. Accessed: Oct. 15, 2017. [Online]. Available: http://spie.org/newsroom/0985-evolution-of-optical-modulation-in-silicon-on-insulator-devices?SSO=1
- [39] S. Tyagi et al., "An advanced low power, high performance, strained channel 65 nm technology," in *IEDM Tech. Dig.*, Dec. 2005, pp. 245–247.
- [40] B. D. H. Tellegen, "The gyrator, a new electric network element," *Philips Res. Rep.*, vol. 3, pp. 81–101, Apr. 1948.
- [41] E. Bogatin, Signal Integrity—Simplified. Englewood Cliffs, NJ, USA: Prentice-Hall, 2003.
- [42] Y.-C. Ou and G. M. Rebeiz, "Differential microstrip and slot-ring antennas for millimeter-wave silicon systems," *IEEE Trans. Antennas Propag.*, vol. 60, no. 6, pp. 2611–2619, Jun. 2012.
- [43] T. Dinc, M. Tymchenko, A. Nagulu, D. L. Sounas, A. Alù, and H. Krishnaswamy, "Synchronized conductivity modulation to realize broadband lossless magnetic-free nonreciprocity," *Nature Commun.*, vol. 8, no. 1, p. 795, 2017. [Online]. Available: https://doi.org/10.1038/s41467-017-00798-9, doi: 10.1038/s41467-017-00798-9.

- [44] Evolution of ULTRACMOS Technology. Accessed: Jul. 11, 2017.
 [Online]. Available: http://www.psemi.com/technologies/ultracmostechnology-platform/evolution-of-ultracmostechnology
- [45] M. Uzunkol and G. M. Rebeiz, "140–220 GHz SPST and SPDT switches in 45 nm CMOS SOI," *IEEE Microw. Wireless Compon. Lett.*, vol. 22, no. 8, pp. 412–414, Aug. 2012.
- [46] B. van Liempd et al., "A +70 dBm IIP3 single-ended electrical-balance duplexer in 0.18 um SOI CMOS," in IEEE Int. Solid-State Circuits Conf. (ISSCC) Dig. Tech. Papers, Feb. 2015, pp. 32–34.



Aravind Nagulu (S'17) received the B.Tech. and M.Tech. degrees in electrical engineering from IIT Madras, Chennai, India, in 2016. He is currently pursuing the Ph.D. degree in electrical engineering with Columbia University, New York City, NY, USA.

During his master's studies, he was involved in the implementation of a high-resolution continuoustime delta-sigma modulator. In 2014, he was an intern with Texas Instruments, Bengaluru, India. His current research interests include exploring new directions to break reciprocity for emerging wireless

communication paradigms and experimental validation of non-reciprocal analog/RF/millimeter-wave integrated circuits and systems.



Tolga Dinc (S'09) received the B.S. and M.S. degrees in electrical engineering from Sabanci University, Istanbul, Turkey, in 2010 and 2012, respectively. He is currently pursuing the Ph.D. degree in electrical engineering with Columbia University, New York City, NY, USA.

In 2015, he was a Design Engineering Co-Op with Texas Instruments, Dallas, TX, USA. In 2016, he was a Research Summer Intern with the IBM T. J. Watson Research Center, Yorktown Heights, NY, USA. His current research interests include

RF/millimeter-wave circuits, antennas, and systems for future wireless applications.

Mr. Dinc was a recipient of several honors and awards, including the 2010 IEEE Microwave Theory and Techniques Society (MTT-S) Undergraduate/Pre-Graduate Scholarship Award, the Sabanci University Gursel Sonmez Research Award in 2012, the 2016 IEEE MTT-S Graduate Fellowship, the 2016 Columbia EE Jacob Millman Prize for Excellence in Teaching Assistance, the IEEE Radio Frequency Integrated Circuits Symposium Best Student Paper Award (First Place) in 2015, and the Columbia EE Jury Award in 2017.



Harish Krishnaswamy (S'03–M'09) received the B.Tech. degree from IIT Madras, Chennai, India, in 2001, and the M.S. and Ph.D. degrees from the University of Southern California (USC), Los Angeles, CA, USA, in 2003 and 2009, respectively, all in electrical engineering.

In 2009, he joined the Electrical Engineering Department, Columbia University, New York City, NY, USA, where he is currently an Associate Professor. In 2017, he co-founded MixComm Inc., a venture-backed startup, to commercialize CoSMIC

lab's advanced wireless research. His current research interests include integrated devices, circuits, and systems for a variety of RF, millimeter-wave, and sub-millimeter-wave applications.

Dr. Krishnaswamy has been serving as a member of the Technical Program Committee of several conferences, including the IEEE International Solid-State Circuits Conference (ISSCC) since 2015 and the IEEE Radio Frequency Integrated Circuits (RFIC) Symposium since 2013. He was a recipient of the IEEE ISSCC Lewis Winner Award for Outstanding Paper in 2007, the Best Thesis in Experimental Research Award from the USC Viterbi School of Engineering in 2009, the Defense Advanced Research Projects Agency Young Faculty Award in 2011, the 2014 IBM Faculty Award, and the 2015 IEEE RFIC Symposium Best Student Paper Award—First Place. He is serving as a Distinguished Lecturer of the IEEE Solid-State Circuits Society over 2017–2018.